

QUANTUM MECHANICAL STUDIES OF NONADIABATIC SYSTEMS

A Dissertation

Presented to the Faculty of the Graduate School
of Cornell University

in Partial Fulfillment of the Requirements for the Degree of
Doctor of Philosophy

by

Eric Gabriel Fuemmeler

May 2018

© 2018 Eric Gabriel Fuemmeler
ALL RIGHTS RESERVED

QUANTUM MECHANICAL STUDIES OF NONADIABATIC SYSTEMS

Eric Gabriel Fuemmeler, Ph.D.

Cornell University 2018

Understanding nonadiabatic processes is tantamount to understanding the mechanisms underlying phenomena such as energy transfer in photovoltaic cells and catalysis at metal surfaces. A complete quantum description of such events is unfortunately intractable, but recent simulations show great promise in approximately but accurately modeling nonadiabatic systems. Perhaps the first step towards modeling these systems is the proper description of the relevant electronic states involved.

We discuss two specific systems in which these states have been calculated, allowing for accurate dynamical simulations to be carried out. The first system described here is a model for intramolecular singlet fission in bipentacenes. Singlet fission, the process by which photoexcited singlet excitons spontaneously split into two lower energy triplet excitons, has received much attention as a promising avenue towards increasing solar cell efficiency. Recently, the blueprint for controlled synthesis of acene dimers has been utilized to create chromophores exhibiting efficient singlet fission, rivaling that of the best crystalline systems. Examining a specific dimer system (2,2-bipentacene), we show that intramolecular singlet fission proceeds nonadiabatically through an avoided crossing between single and multiexcitonic states. Subsequent dynamic calculations reveal singlet fission occurring on ultrafast timescales in agreement with experiment, supporting the proposed mechanism.

Bipentacenes are not only interesting for their singlet fission capabilities, but

also for their unusual spectral features in the visible region. Depending on bonding geometries, the spectrum of bipentacenes can be significantly altered (a second absorption peak appears in the visible) from that of the monomer. Despite first being observed in 1948, this spectral feature has not been properly described. We algebraically detail the origin of this spectral perturbation and give simple design principles for oligoacenes backed by intuitive molecular orbital arguments.

Finally, we discuss a model for energy transfer between diatomics and metal surfaces. Despite being extensively studied experimentally, an adequate theoretical model, accurate across all experimental regimes, has not emerged. Exploiting the simplicity of a Schmidt decomposition of the single particle states of the Newns Hamiltonian, we show how intuitive local states can be constructed and utilized in dynamic calculations.

BIOGRAPHICAL SKETCH

Eric grew up in the small southeastern Missouri town of Farmington. For his undergraduate studies he attended Truman State University in Kirksville, Mo, graduating with a degree in chemistry and a minor in physics. He then moved to Ithaca where he worked under the guidance of Professor Nandini Ananth. During his time in Ithaca, he enjoyed kayaking, hiking and weekend trips to the Adirondacks.

ACKNOWLEDGEMENTS

I want to begin by thanking my research group and in particular my adviser Nandini. I greatly valued our conversations; they were always deeply insightful and encouraging. I also want to thank my family for being nothing but supportive over the past five years. Finally, I must express my gratitude to Lauren. Thank you so much for the love and support.

This work was funded by a National Science Foundation CAREER grant (award no. CHE-1555205) and a Sloan Foundation Fellowship. Parts of Chapter 2 were reproduced from Ref. 1 and Ref. 2 with permissions from the authors. Parts of Chapter 3 were reproduced from Ref. 3 with permissions from the authors.

TABLE OF CONTENTS

Biographical Sketch	iii
Acknowledgements	iv
Table of Contents	v
List of Tables	vii
List of Figures	viii
1 Introduction	1
2 Mechanism of Intramolecular Singlet Fission in Bipentacenes	5
2.1 Survey of Singlet Fission	5
2.1.1 Intramolecular Singlet Fission	9
2.2 Molecule of Interest	11
2.3 Methodologies	11
2.4 Results	16
2.4.1 Monomer Benchmarks	17
2.4.2 Minimal Active Space	17
2.4.3 Towards Quantitative Accuracy	22
2.4.4 Nonadiabatic Pathway	24
2.4.5 Dynamics	27
2.5 Other Molecules	29
2.6 Summary and Future Directions	30
3 Oligoacene Structure-Spectrum Relationships	33
3.1 Observation of Spectral Anomaly	33
3.1.1 Photovoltaic Implications	34
3.2 Spectral Characterization	34
3.2.1 Experimental spectra	35
3.2.2 Pariser-Parr-Pople Theory	35
3.2.3 Reproduction of Spectra	39
3.3 Origin of Second Peak	39
3.3.1 Intensity Borrowing Perturbation Theory	40
3.3.2 Numerical Results	45
3.4 Design Principle	47
3.4.1 Range of Applicability	48
3.5 Summary	51
4 Nonadiabatic Relaxation at Metal Surfaces	52
4.1 Qualitative Mechanism	52
4.2 Model Details	53
4.2.1 Newns Hamiltonian	54
4.2.2 Construction of Diabatic Surfaces	55
4.3 Exact Quantum Dynamics	57

4.3.1	Results	59
4.4	Summary and Future Work	61
5	Conclusions and Future Directions	63
A	Molecular Coordinates	66
B	Normal Mode Analysis Data	86
C	Analytic Fits of Newns Model Potential Energy Surfaces	87

LIST OF TABLES

2.1	Calculated vertical (adiabatic) excitation energies (in eV) of the truncated TIPS-pen molecule	17
2.2	Energies [†] (in eV) and diabatic contributions (%) of the eight lowest adiabatic singlet states	18
2.3	Hamiltonian matrix in the diabatic basis at the 4o4e level (energies in meV).	18
2.4	Comparison between diabatic energies calculated at the 4o4e level of theory in vacuo and using a polarizable continuum model of water.	22
2.5	Hamiltonian matrix in the diabatic basis at the 8o8e level (energies in meV).	22
B.1	$S_0 \rightarrow T_1$ normal mode analysis	86
B.2	$S_0 \rightarrow S_1$ normal mode analysis.	86

LIST OF FIGURES

2.1	A selection of chromophores which exhibit singlet fission: A) tetracene, ⁴ B) pentacene, ⁵ C) tetracyano- <i>p</i> -quinodimethane, ⁶ D) rubrene, ⁷ E) (E,E,E)-1,6-bis(4-fluorophenyl)-1,3,5-hexatriene, ⁸ F) dimer of 1,3-diphenylisobenzofuran. ^{9,10}	6
2.2	Eight lowest energy diabatic configurations represented using the highest occupied molecular orbital (HOMO) and lowest unoccupied molecular orbital (LUMO) on each monomer (A and B). Nomenclature detailed in main text.	7
2.3	Illustration of possible SF pathways beginning in an LE state and ending in the ME state: A) direct pathway, B) mediating mechanism in which secondary state becomes physically populated, C) superexchange mechanism in which mediating state facilitates coupling to first order. In B and C the mediating state depicted is a CT state as is common for SF.	8
2.4	A) The molecule of interest: 22BP. B) Differential transient absorption spectroscopy data for 22BP. C) Isolated singlet and triplet differential photoinduced absorption following a global analysis. The trend observed here is one indication of iSF.	12
2.5	The HOMO of the TIPS-pentacene monomer showing minimal character on the tri-isopropylsilyl groups. Low-lying orbitals of interest show similar distribution across the monomer.	13
2.6	Energies (in eV) of the seven excited diabatic states as a function of dihedral angle (A) and intermonomer bond length (B). Due to degeneracy, the LE, DE, and CT curves each correspond to two diabats as detailed in the text. Each curve is shifted such that the <i>gg</i> diabat at the reference structure (31°, 1.48 Å) is 0 eV.	21
2.7	1435 cm^{-1} monomer mode most strongly coupled to monomer $S_0 \rightarrow S_1/T_1$ electronic transitions.	24
2.8	A) A slice of the potential energy surface along the diagonal of the normal mode coordinate, $\mathbf{Q}=\{Q_1, Q_2\}$, as each substituted pentacene monomer in the dimer relaxes along the 1435 cm^{-1} mode. The values at each point are calculated at the 808e level of theory. The ME state is higher than the LE states at $\mathbf{Q}=(0,0)$, and the avoided crossing is $\mathbf{Q}=(0.33,0.33)$. B) Percent diabatic state composition of the three lowest excited adiabatic states of 22BP as a function of \mathbf{Q} demonstrating strong mixing at $\mathbf{Q}=(0.33,0.33)$ and the change in character of adiabatic states S_1 and S_3 as we move from $\mathbf{Q}=(0,0)$ to $\mathbf{Q}=(1.3,1.3)$	26
2.9	Population evolutions of the three relevant diabats (<i>tt</i> (red), <i>eg</i> (green), <i>ge</i> (blue)) in iSF at $T = 300$ K obtained in our QUAPI simulation.	29

2.10	A collection of bridged bipentacenes. In the bottom representations, the pentacenes are omitted to highlight the nature of the bridging units. Taken from Ref. 2.	31
3.1	Structures of TIPS-pentacene (A), 2,2'-bipentacene (22BP, B), 1,1'-bipentacene (11BP, C) and 2,2'-alkene-linked bipentacene (22eBP, D). On TIPS-pentacene the co-ordinate axes are given along with definitions of short-axis (cata) and long-axis (peri) positions. By each molecule is a picture of an experimental solution in CHCl ₃ , showing how both TIPS-P and 11BP are light blue but 22BP and 22eBP are dark green. The corresponding linear absorption spectra are in Fig. 3.2.	36
3.2	Experimental spectra of TIPS-P (black dashes), 11BP (red), 22BP (blue), and 22eBP (green) taken in CHCl ₃ (A) and corresponding computed spectra (using PPP theory) (B), with insets in the visible region. Although the low-energy transition around 650 nm is virtually unchanged upon dimerization, the yellow box highlights the emergence of a new absorption around 500 nm, seen in 22BP and 22eBP (where it is more intense) but not 11BP. The experimental extinction coefficients and computed spectra are plotted per pentacene to show that 22BP and 22eBP are more absorbent in the visible than the sum of their parts. Computed spectra have linebroadening applied but have not been shifted to agree with experiment and do not include vibrational progressions.	37
3.3	A Top four HOMOs of TIPS-pentacene. Transitions from the HOMO-3 contribute to the intense UV absorption in the monomer and those from the HOMO to a low-energy CT state. B shows how examining nodal structure of orbitals can explain the emergence of an extra absorption. Bonding along a long-axis carbon as for 11BP in B (i) leads to no significant interaction between the HOMO-3 on one monomer and the HOMO on the other. Conversely, bonding via a short-axis carbon as for 22BP in B (ii) leads to a significant orbital interaction. For clarity the dimers are drawn planar and with an elongated inter-monomer bond (thick black line) and long/short axes are defined in Fig. 3.1 A	45
3.4	A) Structure of 66yBP. B) Experimental spectrum showing no second low-energy peak. C) PPP predicted spectrum confirming the absence of the second peak.	47
3.5	Design rule for an extra low-energy absorption in acene derivatives.	48

3.6	<p>Illustrative examples of acene derivatives, showing how in every case the design rule correctly predicts the presence of absence of extra absorption. Left: molecules bonded via a short-axis carbon (blue oval) and without a horizontal (xz) symmetry plane through adjacent monomers, all of which show show enhanced low-energy absorption in their experimental UV-vis spectra. Right: molecules bonded via a long-axis carbon (red oval), or such that the horizontal symmetry plane is preserved through adjacent monomers (red dashes), none of which show enhanced absorption compared to their corresponding monomer(s). The design principle correctly applies to acene dimers, oligomers and polymers such as A,¹¹ B,¹² F,¹³ G¹⁴ and H,¹⁵ complex geometries such as C,¹⁶ I,^{17,18} J¹⁹ and K,²⁰ and to heteroatom-substituted dimers D,²¹ E,²² and L.²³ R denotes a solubilizing or stabilizing group.</p>	49
4.1	<p>A) The neutral diabatic state of the NO-metal surface system. B) The anionic diabatic state of the NO-metal surface. A clear local minimum is present $\sim(1.75,1.20)$. C) The coupling between diabatic surfaces. In all plots the gray curve marks the points at which the two states become degenerate.</p>	58
4.2	<p>$\phi ^2$ projected onto the metal-N coordinate (Z) for a simulation with $E_i=0.1$ eV and $\nu_i=3$. Simulation time increases down the figure. The wavefunction reflects from the surface potential at $Z \simeq 2.5$ Å.</p>	60
4.3	<p>Expectation values of the neutral state population (A), metal-N (Z) distance (B), and N-O (r) distance (C) for three different combinations of initial translational energy (E_i) and initial vibrational states (ν_i) ($E_i=0.1$ eV, $\nu_i=3$ (red), $E_i=0.1$ eV, $\nu_i=15$ (blue), $E_i=0.2$ eV, $\nu_i=3$ (green)).</p>	61

CHAPTER 1

INTRODUCTION

Phenomena such as catalysis at metal surfaces, energy transfer in solar cells, and electron transfer in biochemical complexes, though appearing to be quite different, often proceed through mechanisms involving similar motifs. One particular hallmark of these reactions is the coupling of multiple electronic states with the relevant nuclear degrees of freedom. This nonadiabaticity, though a thorn in the side of experimentalists and theorists alike, is of paramount importance in the proper description of such physical processes. One hopes that by developing accurate models which grant a better understanding of nonadiabatic systems, the rational design of new catalysis, photovoltaic or artificial photosynthetic technologies will be realized.

Theory in particular plays a central role in progressing our understanding of nonadiabatic systems. Such reactions can occur on length and time scales that are difficult to experimentally probe. Furthermore, theory provides absolute control over reaction parameters, often times exploring regimes which may be completely off-limits to modern experiments. Nevertheless, the theoretical characterization of nonadiabatic systems is not without pitfalls. From a quantum dynamical viewpoint, many "standard" approaches fail in the nonadiabatic regime. Much effort has been devoted to alleviating this, with many approximate methods such as mapping variable ring polymer molecular dynamics appearing recently.²⁴ Moreover, purely static electronic properties become more difficult to describe in the nonadiabatic regime.

By definition, multiple electronic states inherently must be considered in nonadiabatic systems. Simple ground state theories must be replaced by ones

which allow for a manifold of states, often (quasi)degenerate, to be treated on equal footing. It is known that excited states often exhibit significantly more static correlation than the ground state, which makes a naive extension of ground state theories to excited states inaccurate.²⁵ In addition, the nuclear modes which facilitate the nonadiabatic interactions may not be known *a priori* and so must be identified. Finally, the basis in which to represent the relevant states must be carefully considered when working in the nonadiabatic regime. Adiabatic states (eigenstates of the electronic Hamiltonian), despite being well defined, are usually not preferred for subsequent dynamic calculations. This is due to the singularities encountered in the evaluation of the nonadiabatic coupling vector defined by Equation 1.1

$$F_{ji} = \frac{\langle \phi_j | \nabla_{\mathbf{R}} H_e | \phi_i \rangle}{E_i - E_j}, \quad (1.1)$$

where \mathbf{R} denotes the nuclear coordinates. Furthermore, when working in the adiabatic representation one must be concerned with the characterization of conical intersections, which is an entire field itself.²⁶

Within the Born-Oppenheimer approximation terms like those in Equation 1.1 are neglected, but as the energies of the electronic states get close (nonadiabatic regime), they cannot be ignored and must be calculated. One is free, however, to rotate from the adiabatic basis into a new (diabatic) basis where the nonadiabatic coupling vector is formally set to 0 and any coupling is moved into the electronic Hamiltonian, causing it to be non-diagonal. This can be seen if the full electronic-nuclear wavefunction is expanded as

$$\Psi(\mathbf{r}, \mathbf{R}) = \sum_k \phi_k(\mathbf{r}; \mathbf{R}) \nu_k(\mathbf{R}) \quad (1.2)$$

with the nuclear Schrödinger equation (once all electronic variables have been

integrated out) expressed as

$$[\mathbf{H}_e(\mathbf{R}) + \bar{\mathbf{F}}(\mathbf{R})]\nu(\mathbf{R}) = E\nu(\mathbf{R}) \quad (1.3)$$

$$[H_e(\mathbf{R})]_{ij} = \delta_{ij}E_i \quad (1.4)$$

with \bar{F} being the nuclear kinetic energy which is comprised of terms like those in Eq. 1.1 and higher order derivatives. Transforming into the diabatic representation, i.e.,

$$\tilde{\phi}_i = \sum_j T_{ij}\phi_j, \quad (1.5)$$

leaves us with

$$[\tilde{H}_e(\mathbf{R})]_{ij} = \langle \tilde{\phi}_i | \hat{H}_e(\mathbf{R}) | \tilde{\phi}_j \rangle \quad (1.6)$$

$$[\tilde{F}(\mathbf{R})]_{ij} = \delta_{ij}f. \quad (1.7)$$

The exact transformation needed to carry out such a diabaticization requires Eq 1.1 to be evaluated which is usually not practical for large systems. Therefore, in most cases, quasi-diabatic states (referred to as simply diabatic states from this point forward) are employed. These states are often physically motivated with simpler constraints, frequently designed to reduce the nonadiabatic coupling in a qualitative sense.²⁷⁻²⁹ Diabatic states are often local in nature, allowing for a more "chemical" interpretation of the problem at hand. The exploitation of this fact is a common theme throughout the work presented here; we will often find it beneficial to view problems through the lens of locality.

We begin this dissertation by first characterizing intramolecular singlet fission in bipentacenes. In Chapter 3 we shift our focus to steady-state properties of biacenes, discussing their structure-spectrum relationships and giving a novel design rule for the creation of highly absorbent chromophores. Chapter 4

focuses on the construction of a model for diatomic-metal interactions, complete with dynamics. Finally, we summarize our work and detail future directions.

CHAPTER 2
MECHANISM OF INTRAMOLECULAR SINGLET FISSION IN
BIPENTACENES

2.1 Survey of Singlet Fission

Singlet fission (SF), the process by which photoexcited singlet excitons spontaneously split into two lower energy triplet excitons, has the potential to be utilized in third-generation of solar cells to surpass the Shockley-Queisser limit of 34% efficiency.^{30,31} This increase in efficiency is partly a result of the two-for-one nature of SF. For every one photon that is absorbed, there are now two excitons capable of diffusing, reaching the interface, and undergoing charge separation. Furthermore, both radiative and nonradiative relaxation pathways are quenched in the triplet manifold—phosphorescence/intersystem crossing are orders of magnitude slower than fluorescence/internal conversion.

Despite the promise, one particular limitation in the implementation of devices exploiting SF is the simple lack of efficient and versatile chromophores which actually undergo SF. To date, there have been relatively few unique chromophores reported to exhibit SF. Thus, it is of paramount importance to understand the detailed mechanism behind SF so that new molecules can be added to the device maker's arsenal.

The first obvious requirement for a molecule to be capable of SF is the energetic criterion, $E(S_1) \geq 2 \times E(T_1)$; that is, in order to observe spontaneous exciton splitting, the overall reaction must be exoergic or near isoergic. This criterion immediately limits the range of SF capable molecules to a small subset of chro-

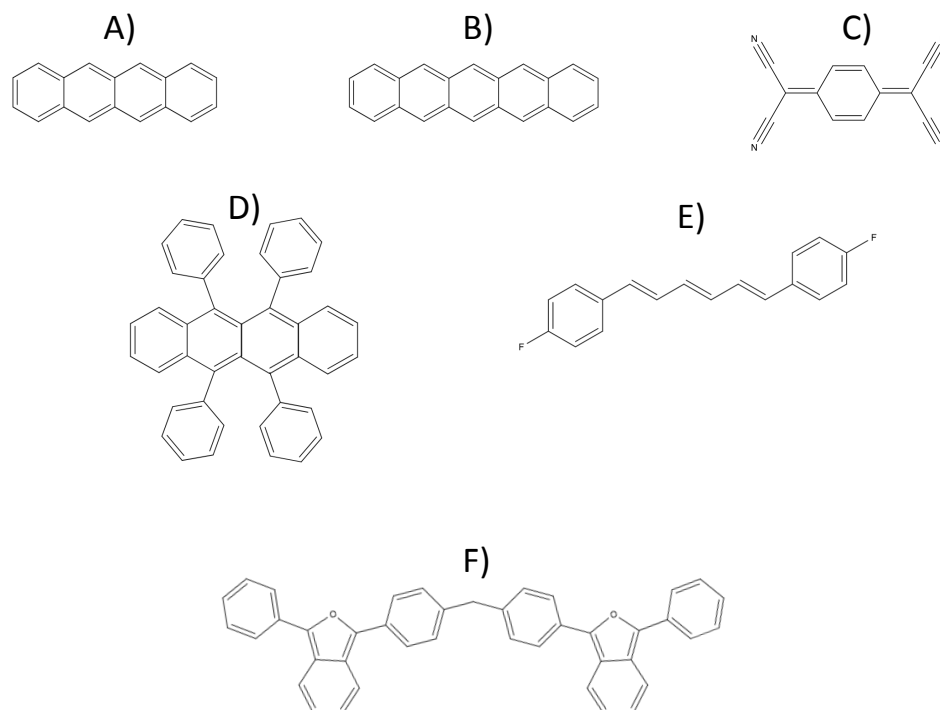


Figure 2.1: A selection of chromophores which exhibit singlet fission: A) tetracene,⁴ B) pentacene,⁵ C) tetracyano-*p*-quinodimethane,⁶ D) rubrene,⁷ E) (E,E,E)-1,6-bis(4-fluorophenyl)-1,3,5-hexatriene,⁸ F) dimer of 1,3-diphenylisobenzofuran.^{9,10}

mophores. Figure 2.1 shows a small selection of SF chromophores.

Energetic considerations alone do not dictate the rate or efficiency of SF. Rather, a more dynamical viewpoint must be taken in order to understand the transient interplay of all states involved. A common starting point for such an analysis is to first describe the electronic states in terms of localized, diabatic states. As mentioned, the use of diabatic states can simplify the interpretation of the problem while allowing for easier implementation of dynamic simulations.

The simplest model for SF one can consider is an interacting dimer system. When analyzed in this way, a number of important localized singlet states have been shown to arise.³¹ These states are pictured in Figure 2.2. The states

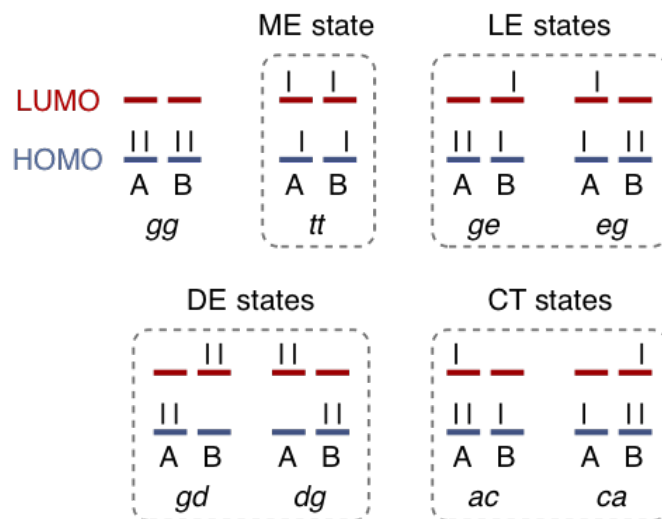


Figure 2.2: Eight lowest energy diabatic configurations represented using the highest occupied molecular orbital (HOMO) and lowest unoccupied molecular orbital (LUMO) on each monomer (A and B). Nomenclature detailed in main text.

labeled *eg* and *ge* are collectively called locally excited (LE) as they each arise from a excitation localized on a single monomer unit, while *gd* and *dg* are local doubly excited states (DE). The state labeled *tt* is a multiexcitonic (ME) state, being comprised of two triplet excitons. Finally, the *ac* and *ca* states are collectively referred to as charge transfer (CT) states.

Having detailed the primary states involved, we are now in position to describe possible pathways for SF. In all cases the ME state will be the target state. Strictly speaking, this state is not the true final product of SF because the excitons are still strongly coupled (for charge separation to occur these excitons must decohere). Nevertheless, it has been common to view this state as the product of the spin-allowed SF process, prior to decoherence. In fact, this idea can help explain why SF occurs on such fast timescales; all states described here are pure singlet states, such that no slow spin symmetry-breaking is required.

Figure 2.3 outlines three possible mechanisms for SF commonly discussed in

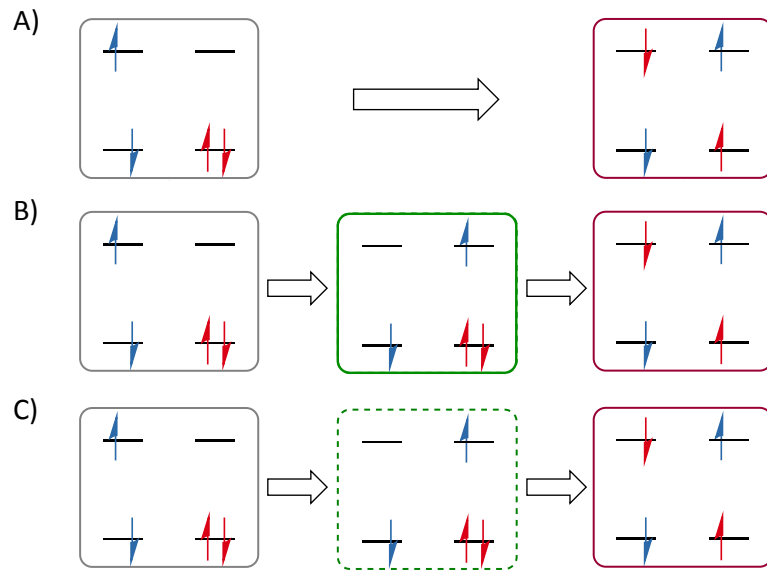


Figure 2.3: Illustration of possible SF pathways beginning in an LE state and ending in the ME state: A) direct pathway, B) mediating mechanism in which secondary state becomes physically populated, C) superexchange mechanism in which mediating state facilitates coupling to first order. In B and C the mediating state depicted is a CT state as is common for SF.

the literature. The first is a “direct” mechanism in which an LE state, following photoexcitation, directly forms the ME state. The second possible mechanism is one in which a secondary state, intermediate in energy, helps facilitate the reaction. This secondary state, though transient, may be measurably populated during the course of SF. The final possible mechanism describes a “superexchange” process, in which a secondary state, though now higher in energy, helps facilitate the reaction. The superexchange mechanism relies on ideas from perturbation theory; the secondary state couples the other two states through a first order effect.

It is often assumed that the direct pathway cannot dominate the SF process. This argument is based on observation that there is very weak coupling

($\sim 1 \text{ meV}$), Equation 2.1, in this scheme.

$$V = \langle LE | \hat{H} | ME \rangle \quad (2.1)$$

Furthermore, there have been few reported instances of the second pathway. This is likely due to the lack of states with energies between that of LE and ME states. There have been a few instances¹⁰ (example shown in Fig. 2.1C), however, in which the CT states appear to be sufficiently stabilized as to allow for an observable two step population transfer. This leaves the superexchange mechanism as the dominant pathway for SF.

Berkelbach *et al*, using a realistic model,³²⁻³⁴ have shown that that the superexchange mechanism can account for the ultrafast SF observed in crystalline pentacene. This is due to an increase in the effective LE-ME coupling. Equation 2.1 can be augmented with an additional term,

$$V_{eff} = \sum_{CT} \frac{\langle ME | \hat{H} | CT \rangle \langle LE | \hat{H} | CT \rangle}{E_{CT} - E_{ME} + E_{CT} - E_{LE}}. \quad (2.2)$$

The matrix elements in Equation 2.2 can be significantly larger in magnitude ($\sim 10 - 100 \text{ meV}$) than Equation 2.1 by virtue of their one-electron nature compared to the smaller two-electron direct coupling. Thus, as long as the energy gaps do not become too large, superexchange can be used to explain ultrafast SF in many cases.

2.1.1 Intramolecular Singlet Fission

Having outlined general SF, we now focus on the specific case of intramolecular singlet fission (iSF), a newer phenomenon only recently reported.^{10,35-39} Unique to iSF, a singlet excited state of a *single* molecule can spontaneously split into

two triplet excitons, occurring even in dilute solution. Unlike intermolecular SF, the mechanism of iSF is independent of nearest neighbor and crystal packing considerations, and instead are dependent on properties that can more robustly be controlled through covalent bonding motifs, such as relative orientation and distance between active portions of the molecule.

Müller *et al.* first reported iSF in a series of benzene bridged tetracene dimers^{35,36} with rather slow fission rates on the order of 10^6 s^{-1} and a maximum fission yield of 3%. They attributed the poor iSF efficiency to the endoergic nature of fission in these molecules, i.e., $E(\text{ME}) > E(\text{LE})$. Aryanpour *et al.* have postulated that low iSF efficiency can be attributed more so to the lack of charge transfer character in the low-lying excited states,⁴⁰ which in the case of crystalline tetracene and other prototypical SF molecules has been shown to be important.⁴¹ They further argue that the analogous bipentacene compounds should exhibit similarly poor iSF despite the exoergic nature of the process in these molecules.

More recently, a number of iSF capable molecules that exhibit fission on much faster timescales have been reported. A small molecule quinoidal bithiophene exhibits iSF on the timescale of a picosecond and with yields as high as 180%.³⁸ In addition, a number of bipentacene molecules have been synthesized and demonstrated to undergo sub-picosecond iSF with yields nearing 200%, in contrast to bitetracene and contrary to theoretical predictions for this group of molecules^{37,42}

The mechanism behind iSF is not entirely clear as many of the usual SF explanations may not be directly transferable. In particular, the role of CT states in mediating iSF seems to be less important compared to conventional SF chro-

mophores. Low-lying CT states are not expected based on the molecular structure, and experimental measurements of iSF rates show relative insensitivity to changes in solvent properties⁴² which are known to affect CT states strongly. It is therefore imperative to understand the details of iSF so that efficient and versatile iSF materials can be designed.

2.2 Molecule of Interest

For the remainder of this chapter much of our focus will be on the recently synthesized triisopropylsilylacetylene (TIPS) substituted 2,2'-bipentacene (22BP) shown in Figure 2.4 along with its transient absorption spectroscopy (TAS) data.^{1,42} The TAS data shows hallmarks of singlet as well as triplet photoinduced absorption. The singlet features rapidly decay with a concomitant increase in the triplet feature. Through a global fitting of the TAS data, it was determined that 22BP undergoes singlet fission with a time constant of 0.76 ps with a yield of 200%, competitive with the best conventional SF chromophores. To gain a better understanding of iSF as well as to be able to compare and contrast to conventional intermolecular SF, we will first carry out a theoretical characterization of the low-lying excited states of 22BP.

2.3 Methodologies

Before detailing the results of our excited state characterization, we will first lay out how the results were obtained. All geometry optimizations were performed at the density functional theory (DFT) level using the B3LYP functional

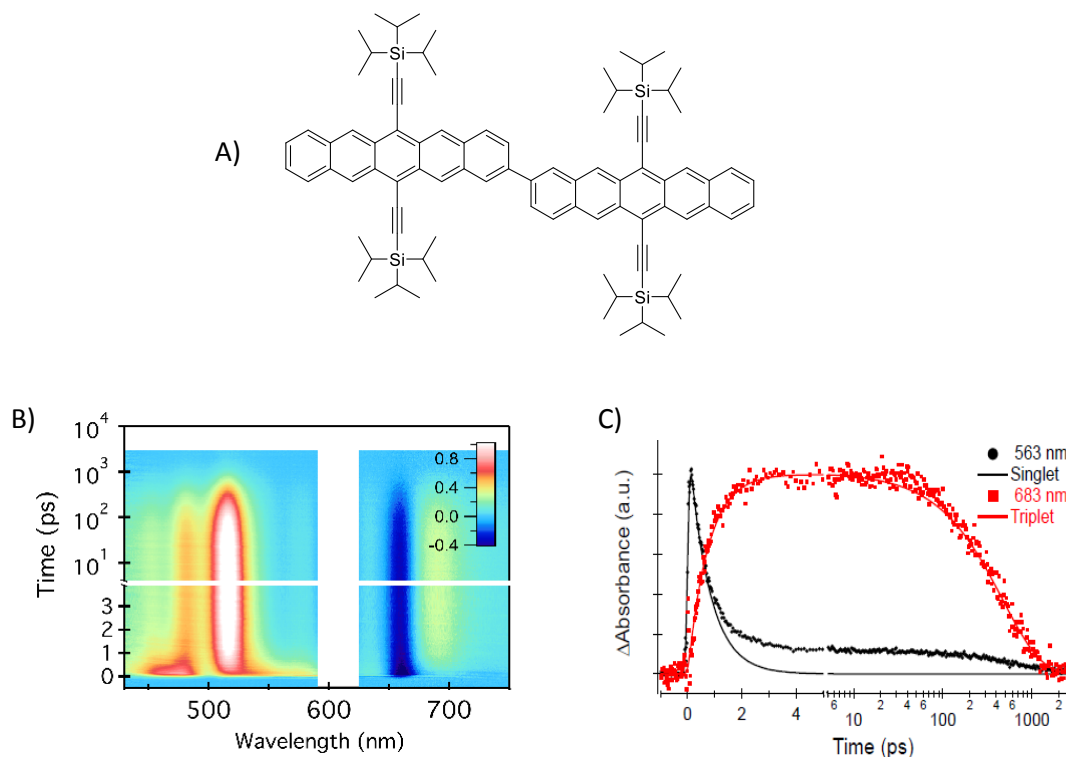


Figure 2.4: A) The molecule of interest: 22BP. B) Differential transient absorption spectroscopy data for 22BP. C) Isolated singlet and triplet differential photoinduced absorption following a global analysis. The trend observed here is one indication of iSF.

and employing the 6-31G* basis set.^{43–45} To facilitate high level calculations, it was found that the structure of 22BP could be simplified by truncating the TIPS groups to include only acetylene units. Figure 2.5 shows a representative frontier orbital of 22BP with nearly no orbital character on the extended TIPS group, which suggests this portion of the dimer will have little effect on the ground and low-lying excited state electronic properties. This conclusion is supported by the work of Kaur *et al.* in their study on the effects of substituents in modifying the electronic structure of pentacene moieties.⁴⁶ Optimized coordinates for 22BP as well other molecules discussed in this text can be found in Appendix A.

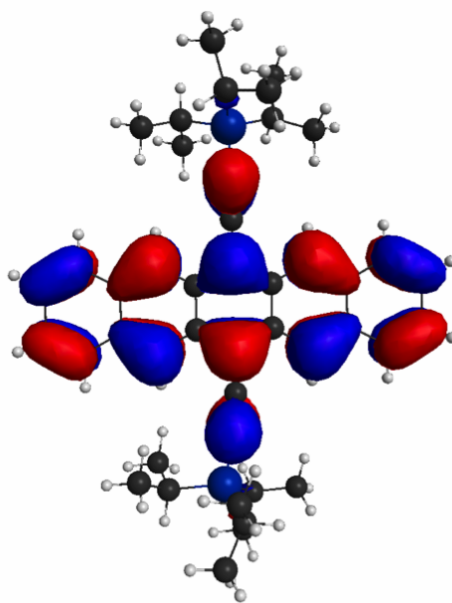


Figure 2.5: The HOMO of the TIPS-pentacene monomer showing minimal character on the tri-isopropylsilyl groups. Low-lying orbitals of interest show similar distribution across the monomer.

Following earlier work on SF in nonbonded pentacene dimers, all excited states were calculated using multireference perturbation theory (MRPT).⁴⁷ Such a theory is necessary for these types of systems in order to properly capture the important static (multireference) and dynamical (perturbation theory) correlation. In particular, a multistate perturb-then-diagonalize MRPT scheme is required to accurately describe states that are (quasi)degenerate, as expected for SF molecules. Specifically, we employ the extended-multiconfiguration quasi-degenerate perturbation theory (XMCQDPT) with a 0.02 au intruder state avoidance shift.⁴⁸⁻⁵¹ We use the SBKJC pseudopotential along with its corresponding double- ζ basis set, plus a d-polarization function for carbons taken from the standard 6-31G* basis.⁵² This particular basis has been shown to provide a proper balance between quantitative accuracy and computational tractability.

We adopt a complete active space (CAS) description to account for static correlation in which all electronic configurations within a restricted subspace of orbitals are allowed. We have found that in order to obtain quantitative accuracy for monomer (dimer) calculations, four (eight) electrons in four (eight) orbitals must be considered. We will, however, still discuss results obtained using smaller spaces. In all cases the selected orbitals are spaced symmetrically about the Fermi level.

Following the solution of the XMCQDPT equations, it is necessary to perform a unitary transformation of the states in order to produce the aforementioned localized states commonly used to interpret SF. This is accomplished using the "4-fold" approach from Nakamura and Truhlar.^{53,54} This procedure invokes the concept of configurational and orbital uniformity to produce smooth diabatic states. Near conical intersections and avoided crossings adiabatic states exhibit rapid changes in their configurational composition. By suppressing these changes across some nuclear coordinate, diabatic states with expected small nonadiabatic coupling can be formed.

As the first step in the procedure one must define a reference geometry (Q) from which a reference set of orbitals and important configuration state functions (CSF's) can be identified. In the context of the localized dimer model for SF this geometry is obvious—it consists of the monomer units separated to non-interacting distances. For the covalent dimer 22BP, dangling bonds can be terminated with hydrogens with their associated basis functions removed. Furthermore, the important CSF's are already known, i.e., those in Figure 2.2. In order to ensure orbital smoothness across a continuous nuclear coordinate, canonical orbitals at Q' can be rotated to maximally overlap with the reference

set, i.e., max D in Equation 2.3 where ξ_i is an atomic orbital and a_i its associated molecular orbital expansion coefficient.

$$D = \sum_{\tau=1}^{N_{orb}} s_{\tau\tau}^2(Q', Q), \quad (2.3)$$

$$s_{\tau\tau}(Q', Q) = \sum_{i=1}^{N_{ao}} \sum_{j=1}^{N_{ao}} a_{\tau i}(Q') a_{\tau j}(Q) \langle \xi_i(Q') | \xi_j(Q) \rangle$$

Expressing each adiabatic state as a linear combination of reference CSF's,

$$\psi_n = \sum_{\alpha \in \{\chi_{ref}\}} \chi_{\alpha} C_{\alpha n} \quad (2.4)$$

and each diabatic state as a combination of adiabatic states,

$$\phi_i = \sum_{n=1}^N \psi_n T_{ni}, \quad (2.5)$$

we arrive at the expression

$$\phi_i = \sum_{\alpha}^A \chi_{\alpha} (\mathbf{C T})_{\alpha i}. \quad (2.6)$$

It is important to note that the truncation of the sum in Equation 2.4 to include only reference CSF's will destroy the unitarity of the transformation matrix \mathbf{T} in Equation 2.6. This truncation usually becomes more significant for higher lying excited states, particularly when employing larger active spaces. We require that all states must be >85% preserved following truncation, which limits the number of adiabatic states that can be included in the analysis.

The transformation matrix, which of course depends on the nuclear coordinate, can be found by maximizing the quantity

$$F = \sum_i (\mathbf{T}^{\dagger} \mathbf{C}^i \mathbf{C}^i \mathbf{T}) \quad (2.7)$$

where the matrix \mathbf{C}^i is defined as

$$C_{\alpha n}^i \equiv C_{\alpha \in \{i\}n}. \quad (2.8)$$

Thus, each diabatic state, ϕ_i , becomes dominated by a single CSF or set of CSF's, $\{\chi_i\}$.

The end product of the diabaticization scheme is a Hamiltonian with matrix elements expressed in the diabatic state basis. From the Hamiltonian one can easily read off each state's energy and their coupling to every other state. We will discuss these diabatic Hamiltonians in more detail in the following sections.

Finally, in order to investigate the effects of solvent polarity on state energetics, diabaticization calculations utilizing the polarizable continuum model (PCM)^{55,56} were performed at the CAS-self-consistent-field (CASSCF) level. A state specific shift, defined as $E(\text{XMCQDPT}) - E(\text{CASSCF})$ *in vacuo*, was applied to the resulting energies to account for the absent dynamical correlation.

All calculations detailed here were performed using the GAMESS-US package.^{57,58}

2.4 Results

We will first discuss benchmark electronic structure calculations for a single monomer unit, before then discussing minimal and larger active space calculations for 22BP. Analysis of dimer results will be simplified by using the previously outlined diabaticization scheme. Finally, important nuclear coordinate modes will be identified to construct a potential energy surface (PES), parts of which are used in a dynamics simulation.

2.4.1 Monomer Benchmarks

For the pentacene moiety we report the excited state energies in Table 2.1 and note that both the 2-orbital-2-electron (2o2e) and 4o4e energies are within 0.05 eV of the experimental energies where available. In addition, we observe the primary energetic criteria for SF, ($E(S_1) > 2 \times E(T_1)$), is met, as expected. Both ${}^3B_{2u}$ and ${}^1B_{2u}$ states are described by a single HOMO to LUMO excitation with a lower excitation energy (adiabatic) than pentacene, attributed to an unusually low LUMO energy.^{46,59} The accuracy of the monomer excited state energies suggests that a 4o4e (2o2e for each monomer) or 8o8e (4o4e for each monomer) dimer calculation is likely to yield similarly accurate results.

Table 2.1: Calculated vertical (adiabatic) excitation energies (in eV) of the truncated TIPS-pen molecule

State	Symmetry	Exp. [†]	4o4e	2o2e
S_1	${}^1B_{2u}$	1.94 (1.84)	2.00 (1.89)	1.94 (1.84)
S_2	1A_g	-	2.33	2.46
T_1	${}^3B_{2u}$	(0.78)	0.95 (0.74)	0.97 (0.76)

[†] Experimental singlet values from Ref. 42 and triplet value from Ref. 37.

2.4.2 Minimal Active Space

The calculated 4o4e energies of the lowest eight states of 22BP are presented in the first column of Table 2.2. We note immediately that the energies are underestimated. In particular the first bright state (the third state in Table 2.2) is experimentally observed at ~ 1.88 eV.⁴² This error is partially carried into the diabatic basis upon rotation.

The Hamiltonian matrix in the 4o4e diabatic basis is shown in Table 2.3. The diagonal elements of the matrix report on the energy of the diabatic states rel-

Table 2.2: Energies [†] (in eV) and diabatic contributions (%) of the eight lowest adiabatic singlet states

Energy	gg	tt	ge	eg	gd	dg	ac	ca
0.00	88.2	0.0	0.0	0.0	5.6	5.6	0.3	0.3
1.53	0.2	97.8	0.0	0.0	0.1	0.1	0.9	0.9
1.67	0.0	0.0	48.4	48.3	0.4	0.4	1.2	1.3
1.69	0.1	0.0	48.7	48.8	1.1	1.1	0.0	0.0
1.86	10.5	0.2	1.2	1.2	43.0	43.1	0.5	0.5
2.01	0.0	0.0	0.4	0.3	49.7	49.6	0.0	0.0
2.81	1.0	2.0	0.0	0.0	0.2	0.2	49.6	47.0
2.81	0.0	0.0	1.3	1.3	0.0	0.0	47.4	50.1

[†] The energies are shifted such that the ground state resides at 0 eV.

ative to the ground state of the dimer while the off-diagonal elements report on the coupling between different diabatic states. These coupling elements are expected to be qualitatively robust with respect to change in active space.⁶⁰ However, we again stress that the diagonal diabatic energies are clearly underestimated. Nevertheless, we may still obtain important conclusions from an analysis of these data.

Table 2.3: Hamiltonian matrix in the diabatic basis at the 4o4e level (energies in meV).

	gg	tt	ge	eg	gd	dg	ac	ca
gg	0.00	-3.00	21.0	21.0	417	417	-164	-164
tt	-3.00	1324	0.10	0.10	23.0	23.0	-125	-125
ge	21.0	0.10	1470	-5.00	22.0	-6.00	-80.0	97.0
eg	21.0	0.10	-5.00	1470	-6.00	22.0	97.0	-80.0
gd	417	23.0	22.0	-6.00	1604	-178	-0.40	-6.00
dg	417	23.0	-6.00	22.0	-178	1604	-6.00	-0.40
ac	-164	-125	-80.0	97.0	-0.40	-6.00	2538	-11.0
ca	-164	-125	97.0	-80.0	-6.00	-0.40	-11.0	2538

The direct coupling matrix element, $\langle tt|\hat{H}|eg/ge\rangle$, is small at <1 meV, comparable to previously reported values for acenes.^{33,41,61,62} Although the magnitudes of the couplings between both the ME and LE states with the CT states, those important to the superexchange mechanism, are comparable to values reported

for pentacene and tetracene dimers,^{33,41,60,61,63} the energetic separation of the CT states is significantly larger. In fact, we find local doubly excited (DE) states, which have not been discussed in the context of SF before, to fall lower in energy than the CT states. This is not entirely unexpected, the second excited state of the monomer possesses marked doubly excited character attributed to the diradical nature of TIPS-pentacene. In contrast, the CT states are shifted higher in energy relative to unsubstituted crystalline pentacene. This effect is also not unexpected – the larger intermonomer separation (monomer center-of-masses separated by 13.6 Å here vs 5 Å in crystalline pentacene) leads to a reduction in the stabilizing Coulomb binding energy and therefore higher CT energies.

As mentioned, previous simulations have shown that higher-lying CT states can participate in fast SF through the superexchange mechanism.^{32–34,41,64} However, CT states separated in energy by > 1 eV from tt exhibit SF on significantly slower timescales.³³ Given the experimentally observed timescales of 760 fs for iSF in 22BP and the large CT energy separation, this suggests a mechanism that is perhaps independent of the CT states.

This conclusion is further supported by the data presented in Table 2.2. In contrast to a number of crystalline acene models^{34,40,61,65–67} we do not observe substantial CT character in any of the lowest six adiabatic states, which would occur if a substantial first order effect is present. Instead, except for S_0 and S_5 , the adiabatic states are all comprised largely of one “type” of diabats. The inherent diradical character of 22BP manifests as a mixing between DE states and the gg state; S_1 is comprised of nearly all tt , while the other states are delocalized and thus exhibit linear combinations of similar types of diabats ($eg + ge$, $dg + gd$, $ac + ca$).

Taken together this data suggests that in order for CT states to become important their energies must be lowered relative to the ME and LE states. There are several mechanisms by which an energy lowering could potentially be realized, e.g. geometric changes and solvent effects. CT is inherently a nonlocal phenomenon, and as such it is expected that CT energy depends strongly upon intermonomer geometry. As suggested by Greyson *et al.*, the dihedral angle can serve as a degree of freedom for tuning the strength of coupling.⁶⁸ When monomers are orthogonal to each other, coupling is expected to be negligible, while for completely planar structures, coupling is at its maximum. Motivated by this and the fact that there are relatively few intermonomer degrees of freedom to adjust due to the direct covalent linking of BP, we examine the dihedral angle's role in modulating CT energies. We perform diabaticization calculations for planar and orthogonal geometries along with several values in between. We observe an increase in couplings overall as the structure becomes more planar. However, the energies of the CT states remain rather constant and high throughout (Figure 2.6A). The increased orbital overlap engendered by planarity cannot overcome the aforementioned unfavorable features contributing to high CT energies.

Along with the dihedral angle, the intermonomer bond distance appears to be one of the few flexible degrees of freedom available. Thus, we perform similar calculations for a variety of bond lengths. Due to unfavorable repulsion at shorter distances, we observe that CT energies are in fact at a minimum near the equilibrium bond length of 1.48 (Figure 2.6B). We conclude that it would take a pronounced intermonomer rearrangement, beyond what is reasonable for 22BP, to sufficiently drive the CT energies low enough to participate in SF.

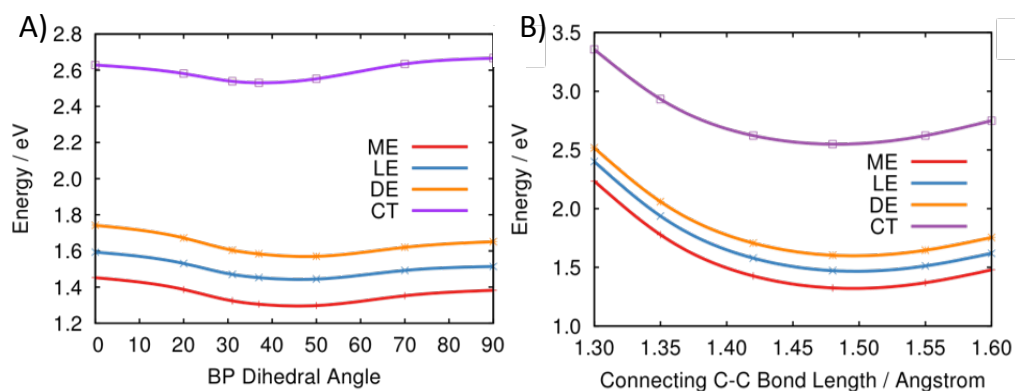


Figure 2.6: Energies (in eV) of the seven excited diabatic states as a function of dihedral angle (A) and intermonomer bond length (B). Due to degeneracy, the LE, DE, and CT curves each correspond to two diabats as detailed in the text. Each curve is shifted such that the gg diabat at the reference structure (31° , 1.48) is 0 eV.

Covalent dimers, perhaps most notably the bianthryl (BA) molecule, have been the subject of a number of studies regarding solvent dependent excited state dynamics.^{69,70} BA displays widely different excited state character and fluorescent dynamics as a function of solvent polarity. This has been attributed to the interplay between excitonic and CT states, facilitated by solvent stabilization of the latter. In the context of iSF a few covalent dimers have similarly shown solvent dependent dynamics.^{10,37} To investigate whether CT energies can be sufficiently lowered in polar solvents, we performed diabaticization calculations employing the polarizable continuum model (PCM) to simulate solvent effects as outlined in section 2.3.

We observe in Table 2.4 that for solvents as polar as water a shift in CT energies relative to all other states is no more than 50 meV. We note that all experiments performed upon 22BP were done so in rather non-polar solvents and without any noticeable change between solvents, supporting our findings. In contrast, a similar bipentacene exhibited solvent dependent iSF dynamics,

which we ascribe to its intermonomer orientation inherently being capable of fostering lower lying CT states.³⁷

Table 2.4: Comparison between diabatic energies calculated at the 4o4e level of theory in vacuo and using a polarizable continuum model of water.

Diabatic State	<i>In Vacuo</i> Energy (eV)	PCM Energy (eV)
tt	1.31	1.32
ge	1.45	1.47
eg	1.46	1.47
gd	1.59	1.60
dg	1.58	1.60
ac	2.51	2.55
ca	2.56	2.55

2.4.3 Towards Quantitative Accuracy

Having questioned the importance of CT states in mediating iSF in 22BP at the 4o4e level, we now turn to the 8o8e level in hopes of achieving quantitative accuracy. Focusing on the four lowest lying states, we now find the energy of the first bright state to be much closer to the experimental value. Table 2.5 shows the Hamiltonian matrix in the diabatic basis.

Table 2.5: Hamiltonian matrix in the diabatic basis at the 8o8e level (energies in meV).

	gg	tt	ge	eg
gg	0.00	-27.0	-18.7	-18.7
tt	-27.0	2010	-2.20	-2.20
ge	-18.7	-2.20	1961	0.80
eg	-18.7	-2.20	0.80	1961

For this larger active space calculation we are unable to explicitly include CT states (or DE for that matter), primarily due to truncation concerns as mentioned in section 2.3. However, we can still identify CT CSF's in the calculated

adiabatic states, but find none within 1 eV of the other states, supporting the findings presented in the previous section. Furthermore, it is very likely that the conclusions reached for the dihedral, bond length, and solvent analyses are equally as valid in this case.

The direct coupling element, although now larger, remains rather small at <5 meV. However, the ME and LE states are quasi-degenerate and as such, a small coupling may still be able to facilitate ultrafast iSF. This small energy separation suggests that a vibronic mechanism may be capable of inducing a change in the character of the lowest singlet state, necessary for efficient iSF.

In order to elucidate if such a mechanism exists we must first identify possible vibronic modes. We do so by projecting the geometric distortions associated with relaxation from the *monomer* ground state to its T_1 and S_1 geometries onto excited state normal modes of the system. The monomer is used to simplify excited state geometry optimizations and hessian calculations. The dimer can be thought of as two weakly coupled monomers and as such each monomer's geometry does not change significantly upon dimerization, justifying the use of a monomer. Furthermore, the dimer normal modes are expected to be simple linear combinations of monomer modes.

The displacement, relaxation energy and Huang-Rhys factor are calculated for each mode with the results tabulated in Appendix B. The Huang-Rhys factor is a measure of a mode's vibrational coupling to an electronic transition given by Equation 2.9,

$$S_i = \frac{m\omega_i Q_i^2}{2\hbar}, \quad (2.9)$$

where ω_i and Q_i denote the i th mode's frequency and displacement, respectively. We identify the mode near 1435 cm^{-1} as the dominant mode in each case,

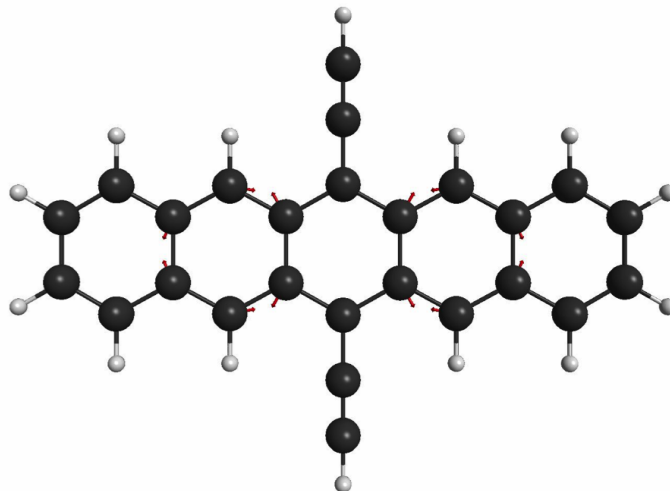


Figure 2.7: 1435 cm^{-1} monomer mode most strongly coupled to monomer $S_0 \rightarrow S_1/T_1$ electronic transitions.

ruling out the low frequency mode near 258 cm^{-1} due to its small relaxation energy. The mode at 1435 cm^{-1} , pictured in Figure 2.7, is a ring-breathing mode. Similar types of modes have been mentioned in SF studies,³³ as these modes are prominent in the vibrational stretching progression of acenes, but they have not been considered in detail.

2.4.4 Nonadiabatic Pathway

We explore the breathing mode by performing XMCQDPT calculations along the 2-D PES spanned by one breathing mode per monomer. Figure 2.8a shows a 1-D cut along the PES where $Q_1 = Q_2$. Starting from the vertical excitation region (denoted 0,0), we observe each excited diabat decreasing in energy along the forward direction of the mode with tt (ME) decreasing the fastest. The initially higher lying ME diabat quickly becomes degenerate with the LE diabats. Near this degeneracy adiabatic states S_1 and S_3 become a coherent superposi-

tion of ME and LE diabats (Figure 2.8b). Despite the overall weak direct coupling strength, as the diabats become sufficiently close in energy, strong mixing occurs. This manifests itself as an avoided crossing between S_1 and S_3 which are each of A symmetry in the C_2 point group. Progressing further along the mode, ME becomes the lowest lying diabat, providing the necessary thermodynamic driving force for singlet fission.

It is important to note that although it appears as if relaxation must occur before SF may proceed, this does not prohibit ultrafast SF. In fact, because the vertical $E(\text{ME}) > E(\text{LE})$, while the relaxed $E(\text{ME}) < E(\text{LE})$ the ME-LE crossing is guaranteed to occur in the forward direction of relaxation, facilitating iSF. We must also highlight that relaxation of the 1435 cm^{-1} mode is near instantaneous compared to the observed timescale of iSF in BP and as such does not inherently slow the process.

Although Figure 2.8 outlines a possible pathway for iSF in 22BP, we cannot determine how fast this process will occur without considering dynamics. To solve this, we detail our exact quantum dynamics calculations in the following section.

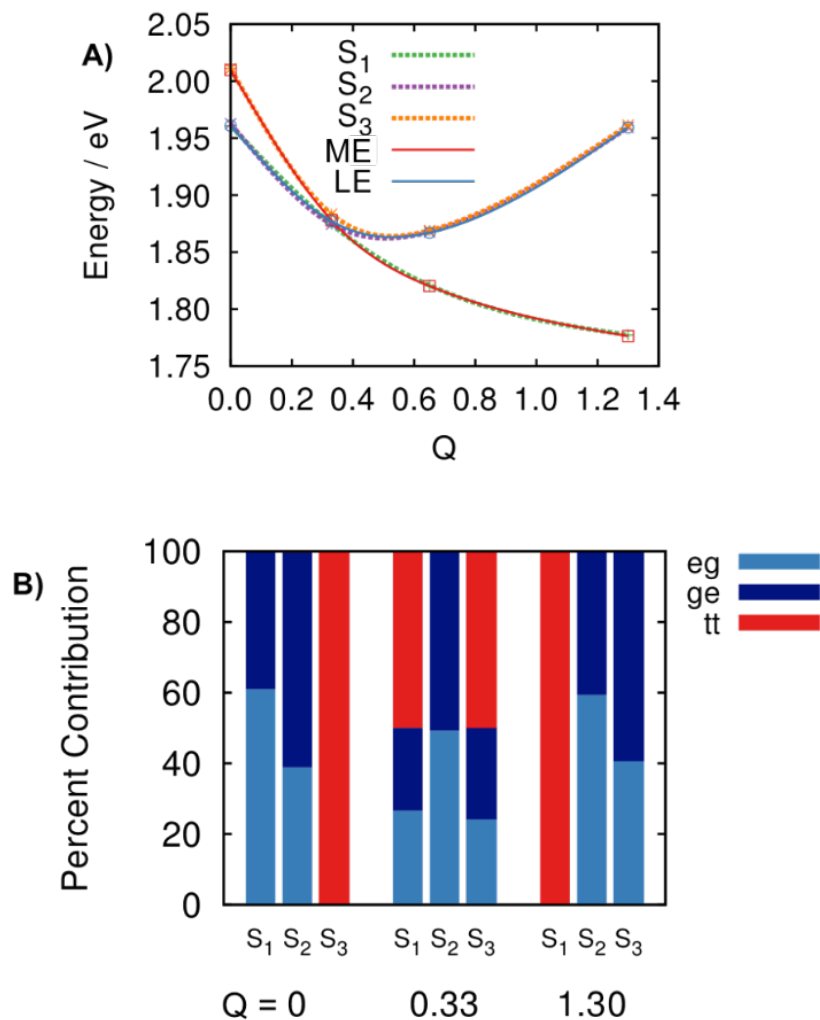


Figure 2.8: A) A slice of the potential energy surface along the diagonal of the normal mode coordinate, $\mathbf{Q}=\{Q_1, Q_2\}$, as each substituted pentacene monomer in the dimer relaxes along the 1435 cm^{-1} mode. The values at each point are calculated at the 8o8e level of theory. The ME state is higher than the LE states at $\mathbf{Q}=(0,0)$, and the avoided crossing is $\mathbf{Q}=(0.33,0.33)$. B) Percent diabatic state composition of the three lowest excited adiabatic states of 22BP as a function of \mathbf{Q} demonstrating strong mixing at $\mathbf{Q}=(0.33,0.33)$ and the change in character of adiabatic states S_1 and S_3 as we move from $\mathbf{Q}=(0,0)$ to $\mathbf{Q}=(1.3,1.3)$

2.4.5 Dynamics

Using the PES minima of each relevant diabat, tt , eg , and ge along the two 1435 cm^{-1} modes, we construct a 2-mode-3-state Hamiltonian as

$$\hat{H}_{ve} = \sum_{n,m}^3 |n\rangle H_{nm} \langle m| + \sum_{i=1}^2 \frac{1}{2} \hbar \omega_c \left(\hat{p}_i + \left(\hat{q}_i - \sum_n^3 |n\rangle q_{i,0}^n \langle n| \right)^2 \right), \quad (2.10)$$

where \hat{H}_{mn} stands for the matrix element of the electronic Hamiltonian between diabats m and n , i.e.,

$$\underline{\underline{H}} = \begin{array}{c} \\ \\ \\ \end{array} \begin{array}{ccc} & tt & eg & ge \\ tt & \left(\begin{array}{ccc} 1.8329 & 0.0045 & 0.0045 \\ 0.0045 & 1.8631 & 0.001 \\ 0.0045 & 0.001 & 1.8631 \end{array} \right) & & \\ eg & & & \\ ge & & & \end{array} \quad (2.11)$$

in units of eV, $\omega_c = 1435 \text{ cm}^{-1}$, \hat{p}_i and \hat{q}_i the dimensionless momentum and position operators of normal mode i , and $q_{i,0}^n$ the minimum of diabat n along mode i . Note that $\frac{1}{2} \hbar \omega_c (q_{i,0}^n)^2$ is the reorganization energy of the diabat n along mode i . The diagonal elements of the \mathbf{H} matrix are the energies of the diabats at their respective minima, i.e., (0.98, 0.98) for tt , (0.98, 0.00) for eg and (0.00, 0.98) for ge , found from a scan of the full 2-D PES spanned by the breathing modes. The off-diagonal elements are taken from the vertical excitation geometry and assumed to be invariant with respect to q_1 and q_2 , while the variations of the diagonal elements are born in the second term of the right-hand-side of Eq. 2.10.

Considering the interaction with solvent molecules, the frequencies of the dominant modes are not sharply defined and it is more appropriate to describe

the model as the three states interacting with a bath of harmonic oscillators:

$$\begin{aligned} \hat{H}_{ve} = & \sum_{n,m}^3 |n\rangle H_{nm} \langle m| + \left(\sum_i \frac{\hat{p}_i^2}{2m_i} + \frac{1}{2} m_i \omega_i^2 \left(x_i - \frac{c_i}{m_i \omega_i^2} \sum_n |n\rangle d_n^1 \langle n| \right)^2 \right) \\ & + \left(\sum_j \frac{\hat{p}_j^2}{2m_j} + \frac{1}{2} m_j \omega_j^2 \left(x_j - \frac{c_j}{m_j \omega_j^2} \sum_n |n\rangle d_n^2 \langle n| \right)^2 \right) \end{aligned} \quad (2.12)$$

i.e., the two modes in Eq. 2.10 are broadened to two sets of modes. The multiplication of c_i and d_n determines the coupling strength of the i^{th} mode and the state n , and the other symbols in Eq. 2.12 are self-explanatory. Note the superscript 1 and 2 for d —it denotes the different couplings between diabats and bath in the two set of modes. We choose to describe the two sets of bath modes using the same Ohmic spectral density:

$$J(\omega) = \frac{\pi}{2} \sum_i \frac{c_i^2}{m_i \omega_i} \delta(\omega - \omega_i) = \frac{\pi}{2} \hbar \omega e^{-\omega/\omega_c}, \quad (2.13)$$

and set

$$d_n^1 = q_{1,0}^n; d_n^2 = q_{2,0}^n. \quad (2.14)$$

In order for the spectral density to peak at ω_c , a description of the broadening, and the reorganization energies (λ) in Eqs. 2.10 and 2.12 are the same, e.g.,

$$\begin{aligned} \lambda_i^n &= \frac{1}{2} \hbar \omega_c (q_{i,0}^n)^2 && \text{(from Eq. 2.10)} \\ &= \frac{(d_n^i)^2}{\pi} \int_0^\infty d\omega \frac{J(\omega)}{\omega}. && \text{(from Eq. 2.12)} \end{aligned} \quad (2.15)$$

Using Equation 2.12, we can employ the QUasi-Adiabatic Path Integral (QUAPI) method for solving the quantum dynamics of our iSF model. See Refs. 71–75 for details, but briefly, QUAPI carries out exact quantum dynamics for systems coupled to a bath, our broadened modes in this case. The calculations are made tractable by exploiting the loss of coherence induced by bath interactions. Simulations can therefore be converged with respect to a truncation of the so-called "memory kernel".⁷³

We choose $T = 300$ K in our QUAPI simulation as the experiment is conducted under room temperature, and the simulation converges with the time step of 5.92 fs and 12 steps of memory time ($12 \times 5.92 = 71.04$ fs). The simulation starts with a density matrix occupying only the eg diabat and the evolutions of population of all three states are calculated. The results are shown in Figure 2.9. The timescale for the rise-up of the tt population is about 500 fs, which is in satisfactory agreement with the experimental observation (about 700 fs).

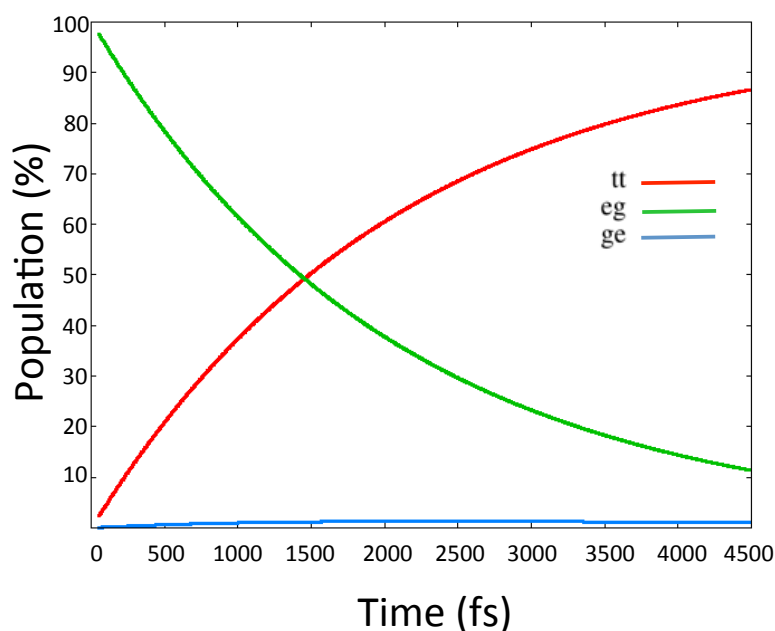


Figure 2.9: Population evolutions of the three relevant diabats (tt (red), eg (green), ge (blue)) in iSF at $T = 300$ K obtained in our QUAPI simulation.

2.5 Other Molecules

The theory of iSF in 22BP can readily be applied to explain observed iSF trends in a variety of similar bipentacene compounds. For example, a 2,2'-diphenyl derivative of 22BP has been observed to undergo singlet fission on timescale of 3.38 ps. Qualitatively we can attribute this decrease in rate compared to

22BP to its increased intermonomer dihedral angle ($\sim 57^\circ$ vs. $\sim 37^\circ$). As previously mentioned, an increase in the dihedral angle serves to decrease coupling and we find the direct coupling to be approximately half that of 22BP. Invoking Fermi's golden rule, which proportions the rate to the coupling squared, we can predict a four-fold slow down in iSF, which is quite close to the observed ~ 4.5 times slow down. Finally, we note that iSF is not restricted to occur only in directly linked dimers, but instead has also been observed in systems possessing linkers between monomers.² As long as these linkers are capable of facilitating adequate coupling between monomer units, ultrafast iSF can still occur. A collection of such molecules can be found in Figure 2.10, which include an ethanobenzo[*b*]-decacene derivative (EBD), a spirobi[cyclopenta[*b*]-pentacene] derivative (Spi), a bistrifluoromethyl derivative (TFM), a bicyclooctane linked dimer (BCO), and a phenyl linked dimer (BP-1).

2.6 Summary and Future Directions

In this chapter we have detailed iSF in bipentacenes. In particular, aided by theory, we found a novel mechanism for ultrafast iSF in 22BP: direct coupling of the LE and ME states facilitated by vibronically induced degeneracy. We identified the dominant vibronic coupling mode as a symmetric ring-breathing mode. Furthermore, we ruled out significant contributions of a CT mediated mechanism, unlike in the case of conventional SF. Accurate dynamic calculations and characterization of iSF rates of molecules with different dihedral angles confirms the robustness of the direct coupling mechanism.

In the future it may be interesting to investigate an asymmetric mode in

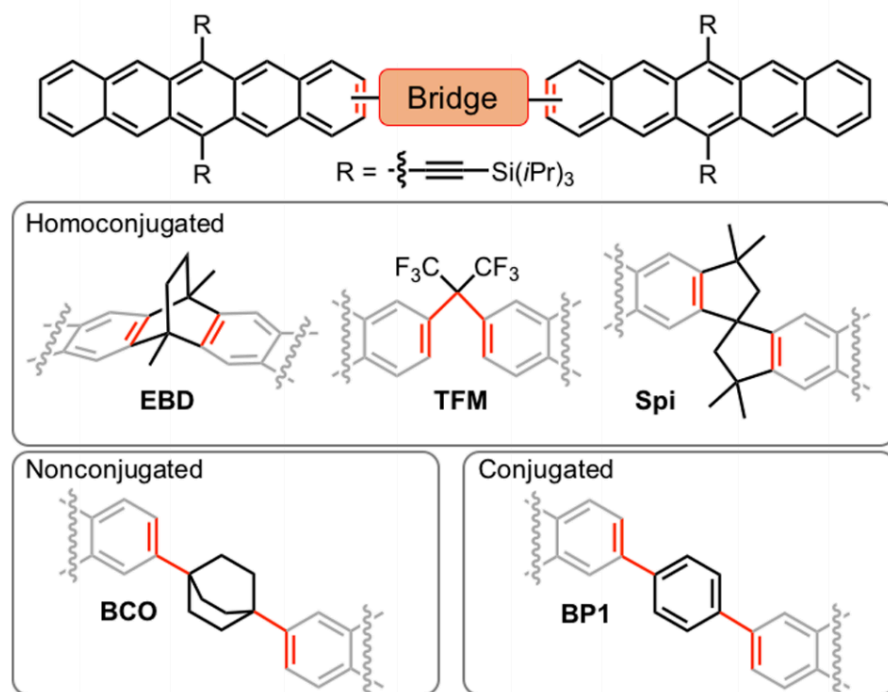


Figure 2.10: A collection of bridged bipentacenes. In the bottom representations, the pentacenes are omitted to highlight the nature of the bridging units. Taken from Ref. 2.

conjunction with the one explored here. If the symmetry of the chromophore is strictly preserved, the spectroscopically bright adiabatic state will usually be of different symmetry to the primarily ME adiabatic state. Thus, a symmetry-breaking mode must be considered to observe population transfer between the two. It may also be necessary to reevaluate CT energies using different active spaces. As suggested in the work discussed in next chapter, the HOMO-1/LUMO+1 may not be the most important orbitals to include in the dimer 808e active space. Finally, it would be interesting to apply the ideas presented here for the study of triplet-triplet recombination. This process understandably occurs quickly in iSF chromophores, but in order to achieve successful charge separation, this pathway should be suppressed. Perhaps a chromophore could be designed such that recombination can be shut off through a geometric rear-

rangement following SF.

CHAPTER 3

OLIGOACENE STRUCTURE-SPECTRUM RELATIONSHIPS

Investigation of the electronic structure and spectra of organic molecules has a long history, dating back to the molecular orbital theories of Hückel⁷⁶ and the oscillator strength sum rules of Thomas, Reiche and Kuhn.⁷⁷⁻⁷⁹ These have been followed by development and application of more sophisticated electronic structure methods^{47,80-86} and the formulation of structure-spectrum design principles such as Kasha's point dipole model,⁸⁷ crystallochromy,⁸⁸ and the tuning of absorption frequencies (color) by alteration of orbital energy gaps.⁸⁹ Despite considerable progress, there remains a need for more systematic design rules for the creation of absorbent and tunable chromophores.⁹⁰⁻⁹²

3.1 Observation of Spectral Anomaly

Their potential for SF has led to the synthesis and characterization of a huge range of dimers and oligomers of tetracene and pentacene similar to 22BP. Some of these molecules have been found to exhibit a second intense low-energy absorption in addition to the monomer-like $S_0 \rightarrow S_1$ transition^{42,93,94} whereas others have not.⁹⁵ This new extra absorption occurs without any significant change in intensity or frequency of the lower energy transition, which is preserved in all these dimers.^{42,93-95} Examining the literature, we find that the first observation of a second low energy peak in acene systems occurred in 1948 for dimers of naphthalene (where all the transitions are in the UV,⁹⁶) and has been more frequently observed in recent times as these types of compounds increase in popularity.^{12,16,21,22} Previous computational investigations have assigned this as

a $\pi \rightarrow \pi^*$ transition^{11,12} but there has been no clear explanation of its presence in some acene derivatives^{12,16,21,22,96} and absence in others.^{13–15,17–20,23}

3.1.1 Photovoltaic Implications

While seemingly a curiosity, the ability to synthesize acene derivatives which have enhanced visible absorption but whose photophysics are otherwise unaffected has the potential to increase the efficiency of organic photovoltaics, where one limitation is the short exciton diffusion length compared to absorption length.⁹⁷ In theory, using a more absorbent chromophore would allow for a decrease in the thickness of a cell while still absorbing the same proportion of solar radiation (thereby reducing cost and increasing flexibility). Furthermore, the thinner cell would allow more diffusing excitons to be extracted as current, increasing efficiency. There is consequently a theoretical and practical need to explain the origin of this new absorption and predict in what acene derivatives it will, and will not, occur.

3.2 Spectral Characterization

The spectra of acenes is a large and much-studied area (see e.g. Refs. 15,47, 66,83–86,98–108) and here we focus on the particular case of forming covalent dimers and oligomers of acenes. Although we find our results to be widely applicable, we present them in the context of TIPS-pentacene, Fig. 3.1A), the monomer unit comprising 22BP.

3.2.1 Experimental spectra

We first consider the experimental spectra of TIPS-pentacene as well as 22BP, a 1,2'-bipentacene (12BP), and an ethene linked bipentacene (22eBP) with molecules shown in Fig. 3.1 and spectra in Fig. 3.2. The spectrum of TIPS-pentacene shows the familiar features of an acene spectrum:^{83,84,103} a weak y-polarized transition at low frequencies (co-ordinates defined in Fig. 3.1A), accompanied by a vibrational stretching progression commonly seen in the electronic spectra of organic molecules. There is also a very intense absorption in the near UV (310 nm). We see that in 22BP there is a new absorption in the visible, with perturbations in the UV, sufficiently intense to turn the dimer color from blue to dark green. Perhaps surprisingly, the lowest-energy transition (S_1) is unaffected by dimerization and has no significant red or blue-shift. The extinction coefficients are plotted per pentacene to show that, in the visible, the 2,2' dimer is more absorbent than the sum of its parts and it is not an artifact of the chromophore being twice as large. The spectrum of 22eBP also exhibits the second low-lying peak, being even more intense, while 11BP does not. In fact, the spectrum of 11BP simply resembles that of the monomer.

3.2.2 Pariser-Parr-Pople Theory

To understand the experimental spectra of TIPS-pentacene and its dimers, we wish to compute their spectra. Since these are large chromophores, and we wish to make general predictions about structure-spectrum relationships, we desire a theory sufficiently sophisticated that it can capture the qualitative features of the excited-state spectra, but sufficiently simple to allow for a chemically intuitive

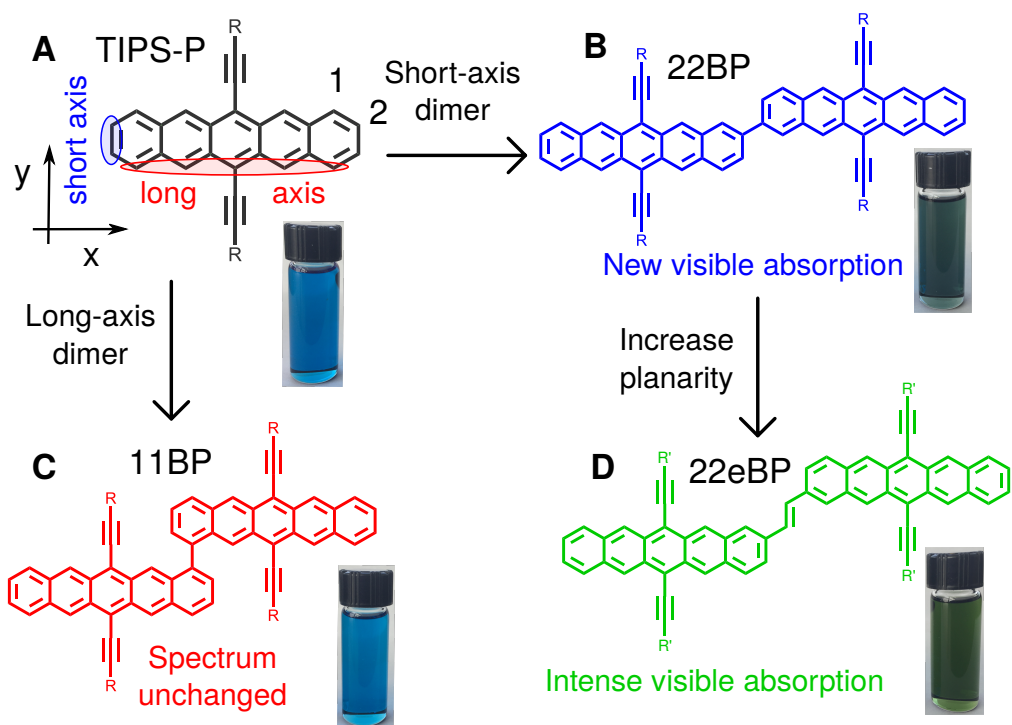


Figure 3.1: Structures of TIPS-pentacene (A), 2,2'-bipentacene (22BP, B), 1,1'-bipentacene (11BP, C) and 2,2'-alkene-linked bipentacene (22eBP, D). On TIPS-pentacene the co-ordinate axes are given along with definitions of short-axis (cata) and long-axis (peri) positions. By each molecule is a picture of an experimental solution in CHCl₃, showing how both TIPS-P and 11BP are light blue but 22BP and 22eBP are dark green. The corresponding linear absorption spectra are in Fig. 3.2.

interpretation. We therefore choose Pariser-Parr-Pople (PPP) theory,^{80,83,109-111} which was developed for the calculation of low-lying excited electronic states of conjugated systems.^{80,83} Its similarity to simple molecular orbital (MO) theories such as Hückel theory allows for a chemically intuitive interpretation of results.^{109,110} Unlike Hückel theory, however, PPP theory includes two-electron interactions (within the neglect of differential overlap (NDO) approximation) such that it correctly accounts for Coulomb and exchange interactions which are required to give accurate excited state energies.⁸²

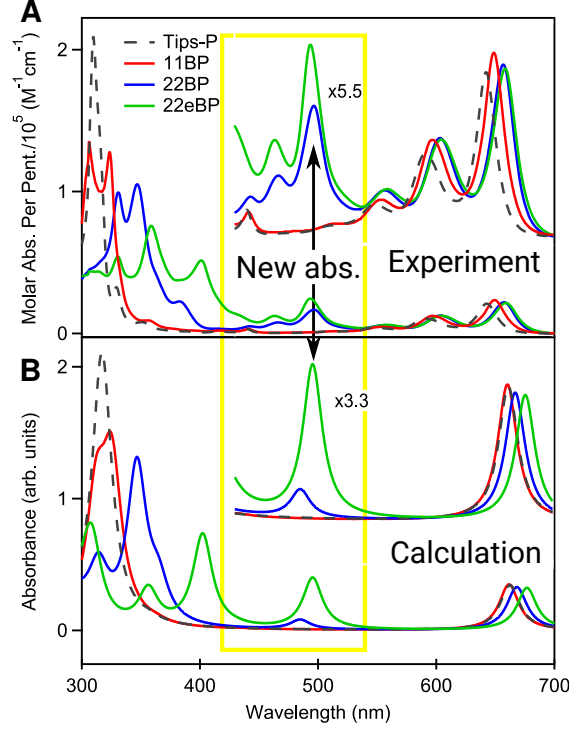


Figure 3.2: Experimental spectra of TIPS-P (black dashes), 11BP (red), 22BP (blue), and 22eBP (green) taken in CHCl_3 (A) and corresponding computed spectra (using PPP theory) (B), with insets in the visible region. Although the low-energy transition around 650 nm is virtually unchanged upon dimerization, the yellow box highlights the emergence of a new absorption around 500 nm, seen in 22BP and 22eBP (where it is more intense) but not 11BP. The experimental extinction coefficients and computed spectra are plotted per pentacene to show that 22BP and 22eBP are more absorbent in the visible than the sum of their parts. Computed spectra have linebroadening applied but have not been shifted to agree with experiment and do not include vibrational progressions.

The overall PPP Hamiltonian is^{80–83,112}

$$\begin{aligned}
 \hat{H} = & \sum_{\mu} \epsilon_{\mu} \hat{n}_{\mu} + U_{\mu\mu} \hat{n}_{\mu,\uparrow} \hat{n}_{\mu,\downarrow} + \sum_{\mu < \nu} \sum_{\sigma} t_{\mu\nu} (\hat{a}_{\mu\sigma}^{\dagger} \hat{a}_{\nu\sigma} + \hat{a}_{\nu\sigma}^{\dagger} \hat{a}_{\mu\sigma}) \\
 & + \sum_{\mu < \nu} V_{\mu\nu} (\hat{n}_{\mu} - Z_{\mu}) (\hat{n}_{\nu} - Z_{\nu})
 \end{aligned} \tag{3.1}$$

where \hat{n}_μ is the number operator for the number of electrons on atom μ ,

$$\hat{n}_\mu = \sum_{\sigma=\{\uparrow,\downarrow\}} \hat{n}_{\mu,\sigma}, \quad (3.2)$$

$$\hat{n}_{\mu,\sigma} = \hat{a}_{\mu,\sigma}^\dagger a_{\mu,\sigma}, \quad (3.3)$$

and $\hat{a}_{\mu,\sigma}^\dagger, \hat{a}_{\mu,\sigma}$ are the creation and annihilation operators respectively for an electron of spin σ on atom μ . ϵ_μ is the on-site energy, which for a purely hydrocarbon chromophore we can set to zero without affecting the energies of excited states, $U_{\mu\mu}$ is the on-site (Hubbard) repulsion, and $V_{\mu\nu}$ is the parameterized repulsion between an electron on atom μ and an electron on atom ν . Consistent with convention,⁸³ we use Greek letters to denote atomic orbitals $\{\chi_\mu\}$ and Roman letters to denote molecular orbitals $\{\phi_i\}$.

The hopping parameter $t_{\mu\nu}$ was set to -2.2 eV for single bonds, -2.4 eV for aromatic bonds, and -2.8 eV for triple bonds, scaled by a cosine of the dihedral angle for inter-monomer bonds.¹¹³ For highly non-planar molecules, other NDO methods such as INDO could be used for spectral prediction^{91,114} but we find PPP theory sufficiently accurate. The electronic repulsion terms were parameterized using the Mataga-Nishimoto form:¹¹⁵ $V_{\mu\nu} = U/(1 + \frac{R_{\mu\nu}}{r_0})$ where the Hubbard $U = 8$ eV and $r_0 = 1.634$ Å. For plotting the results of PPP calculations, the excited state energies were not shifted to agree with experiment. Peaks were broadened using a full width at half maximum value of 20 nm, and do not include vibrational progressions. PPP calculations were performed using in-house code finding the lowest 25 singly excited states.

3.2.3 Reproduction of Spectra

We see that the PPP spectra, Fig. 3.2B are in good agreement with experimental spectra and correctly predicts an extra absorption in 22BP and 22eBP that is not present in the monomer. The extra peak in 22BP is somewhat weaker and slightly blue-shifted compared to experiment, whereas the extra peak in 22eBP is accurately captured, both in terms of absorption frequency and relative intensity. We also see that PPP correctly predicts a Davydov splitting of the 11BP absorption (seen as a peak with a shoulder around 320 nm) and a diminution in the height of the UV peaks although their relative intensities are inaccurate for 22BP and 22eBP.

We find the excitation around 650 nm is mainly HOMO→LUMO, and the intense UV peak an in-phase combination of HOMO-3 to LUMO and HOMO to LUMO+3, whose corresponding out-of-phase combination is dark in PPP theory and very weakly absorbent in experiment around 440 nm. Excitations from the HOMO-1 to LUMO and HOMO to LUMO+1 are dipole forbidden, and the excitations from the HOMO-2 to the LUMO and the HOMO to the LUMO+2 are predicted by PPP theory to be y-polarized, giving a dark out-of-phase state at 358 nm and a bright in-phase state at 366 nm which appears as a shoulder in the intense UV absorption seen experimentally around 350 nm.

3.3 Origin of Second Peak

Although we find PPP theory to accurately predict the presence or absence of the second low-energy peak, it alone does not suffice to explicitly explain the

phenomenon. Therefore, in order to algebraically elucidate the origin of the extra bright peak, we will combine the machinery of intensity borrowing perturbation theory with the PPP Hamiltonian.

3.3.1 Intensity Borrowing Perturbation Theory

We first formally define our system in the language of perturbation theory. Similar to Kasha,⁸⁷ for two monomers N and M we define our Hamiltonian

$$\hat{H} = \hat{H}_N + \hat{H}_M + \hat{V} \quad (3.4)$$

where \hat{H}_N and \hat{H}_M are the Hamiltonians of the monomers at infinite separation and our zeroth-order Hamiltonian is therefore $\hat{H}_0 = \hat{H}_N + \hat{H}_M$. Kasha approximated \hat{V} as a dipole-dipole interaction and assumed all excitations were intramonomer,⁸⁷ but here we make no *a priori* assumptions about the nature of the excitations nor the functional form of \hat{V} . Instead, we choose to describe the overall system using PPP theory⁸⁰⁻⁸³ which we have already shown provides an accurate description of the electronic structure of these molecules.

To define the monomer Hamiltonians, we let \mathcal{M} be the set of atoms on monomer M and likewise for \mathcal{N} on monomer N , such that

$$\begin{aligned} \hat{H}_M = & \sum_{\mu \in \mathcal{M}} \epsilon_{\mu} \hat{n}_{\mu} + U_{\mu\mu} \hat{n}_{\mu,\uparrow} \hat{n}_{\mu,\downarrow} + \sum_{\mu < \nu \in \mathcal{M}} \sum_{\sigma} t_{\mu\nu} (\hat{a}_{\mu\sigma}^{\dagger} \hat{a}_{\nu\sigma} + \hat{a}_{\nu\sigma}^{\dagger} \hat{a}_{\mu\sigma}) \\ & + \sum_{\mu < \nu \in \mathcal{M}} V_{\mu\nu} (\hat{n}_{\mu} - Z_{\mu})(\hat{n}_{\nu} - Z_{\nu}) \end{aligned} \quad (3.5)$$

and likewise for monomer N , where $\sum_{\mu < \nu \in \mathcal{M}}$ is taken to mean summing over atoms μ on monomer M and atoms ν on monomer M , provided that $\mu < \nu$.

Combining Eq. (3.5) and Eq. (3.4) we find

$$\begin{aligned}\hat{V} &= \hat{H} - \hat{H}_0 \\ &= \sum_{\mu \in \mathcal{M}, \nu \in \mathcal{N}} \sum_{\sigma} t_{\mu\nu} (\hat{a}_{\mu\sigma}^\dagger \hat{a}_{\nu\sigma} + \hat{a}_{\nu\sigma}^\dagger \hat{a}_{\mu\sigma}) + \sum_{\mu \in \mathcal{M}, \nu \in \mathcal{N}} V_{\mu\nu} (\hat{n}_\mu - Z_\mu) (\hat{n}_\nu - Z_\nu)\end{aligned}\quad (3.6)$$

This procedure is similar in spirit to that previously used to construct inter and intra-monomer contributions to Hamiltonians in large systems^{40,112,116} and here we apply it perturbatively to chromophore design.

As the two chromophores are noninteracting at infinite separation, we can solve \hat{H}_N and \hat{H}_M separately for their corresponding molecular orbitals. Because the monomers are identical, each orbital will be degenerate with the same orbital on the other monomer, and we therefore choose the degenerate orbitals such that they are localized entirely on monomer N or monomer M . We can therefore formally define the orbitals as ϕ_{ni} or ϕ_{mi} where n or m denotes an orbital on monomer N or M respectively and i, j, k, l are indices for MOs. In accordance with convention⁸³ orbitals are numbered $1, 2, 3, \dots$ from the HOMO downwards and $1', 2', 3', \dots$ from the LUMO upwards. As noted by Pariser,⁸³ care must be taken to be consistent with the relative signs of orbitals in order for the Coulson-Rushbrooke theorem, which states that the π -orbitals are spaced symmetrically about the zero of energy with each symmetric pair possessing equal but opposite orbital amplitude at every other atomic position,¹¹⁷ to be easily applied. For the dimers considered here we choose every monomer orbital to have the same sign on the atom through which it is joined to the other monomer.

As we are interested in the linear absorption spectra and the dipole moment is a one-electron operator, we consider only singly excited states, as in the original formulation of PPP. We denote single excitations $|\Phi_{xi}^{yj}\rangle$ where x and y are either n or m , and here we only consider singlet spin-adapted configurations¹¹⁸ as

triplet excitations are dark for hydrocarbons with minimal spin-orbit coupling.

We have two types of single excitations, where either $x = y$ or $x \neq y$. The first variety, $|\Phi_{ni}^{nj'}\rangle$ or $|\Phi_{mi}^{mj'}\rangle$, are intramolecular, Frenkel excitations. For alternant hydrocarbons^{80,83,117} such as the molecules considered in this article, $|\Phi_{ni}^{nj'}\rangle$ and $|\Phi_{nj}^{ni'}\rangle$ are degenerate and we therefore define ‘plus’ and ‘minus’ excitations⁸³

$$|\Phi_{ninj}^{\pm}\rangle = \frac{1}{\sqrt{2}}(|\Phi_{ni}^{nj'}\rangle \pm |\Phi_{nj}^{ni'}\rangle) \quad (3.7)$$

where only ‘plus’ excitations have nonzero transition dipole moment from the ground state, and $|\Phi_{ni}^{ni'}\rangle =: |\Phi_{nini}^+\rangle$.⁸³

The second type of excitation is $|\Phi_{ni}^{mj'}\rangle$ or $|\Phi_{mi}^{nj'}\rangle$, which are intermolecular, charge-transfer (CT) excitations.^{30,66,119} Using the definition of the dipole moment in PPP theory⁸³ and the fact that orbitals on different monomers are spatially disjoint, CT excitations are always dark ($\langle\langle\Phi_0|\hat{\mu}|\Phi_{ni}^{mj'}\rangle\rangle = 0$) and have diagonal energy

$$\langle\langle\Phi_{ni}^{mj'}|\hat{H}_0|\Phi_{nk}^{ml'}\rangle\rangle = \delta_{ik,j'l'}(f_{mj'mj'}^{(0)} - f_{nini}^{(0)}) \quad (3.8)$$

where $f_{mj'mj'}^{(0)}$ is the (diagonal) element of the zeroth-order Fock matrix corresponding to the energy of orbital mj' .

This means that the zeroth order eigenstates will be monomer Frenkel excitations (each of which will be degenerate with the same excitation on the other monomer) and charge-transfer excitations (which will also be at least doubly degenerate). The only bright states at zeroth order will be PPP ‘plus’ Frenkel excitations. For simplicity in what follows, we assume zeroth-order Frenkel states to be dominated by a single PPP ‘plus’ or ‘minus’ state.

Having obtained zeroth-order eigenstates of \hat{H}_0 , we now consider how they

are mixed by the perturbation \hat{V} which occurs upon bonding two monomers together, and how this alters the linear absorption spectrum. As in standard perturbation theory,¹²⁰ we form the ‘good’ degenerate eigenstates of \hat{H}_0 as linear \pm combinations of excitations which we denote A and B in accordance with the irreducible representations (irreps) of the C_2 point group, of which the molecules of interest are members.¹²⁰ For Frenkel excitations we have

$$|F_{ij}^{A,\pm}\rangle = \frac{1}{\sqrt{2}}(|\Phi_{ninj}^\pm\rangle + |\Phi_{mimj}^\pm\rangle), \quad (3.9a)$$

$$|F_{ij}^{B,\pm}\rangle = \frac{1}{\sqrt{2}}(|\Phi_{ninj}^\pm\rangle - |\Phi_{mimj}^\pm\rangle), \quad (3.9b)$$

and for CT

$$|CT_{ij}^A\rangle = \frac{1}{\sqrt{2}}(|\Phi_{ni}^{mj'}\rangle + |\Phi_{mi}^{nj'}\rangle), \quad (3.10a)$$

$$|CT_{ij}^B\rangle = \frac{1}{\sqrt{2}}(|\Phi_{ni}^{mj'}\rangle - |\Phi_{mi}^{nj'}\rangle), \quad (3.10b)$$

and is similar to the linear combinations used in (for example) Kasha exciton theory,⁸⁷ though Kasha only considered Frenkel excitations interacting via a dipole-dipole interaction. Note that in certain cases of degeneracy further linear combinations may be required but we do not find this necessary in what follows, and if there is ‘strong’ coupling or near-degeneracies (where the energy gap is comparable to the coupling between states) then quasidegenerate perturbation theory¹²¹ can be used.

For a relatively flat molecule such as 22BP (close to C_{2h} symmetry), only the B irreps will have substantial oscillator strength, and since the perturbation \hat{V} is symmetric under all symmetry operations of the dimer, only like irreps can mix. From the PPP results, we are interested in the UV Frenkel excitation $|F_{14}^{B,+}\rangle$ mixing with the dark charge-transfer excitation $|CT_{11}^B\rangle$, and using standard elec-

tronic structure theory algebra¹¹⁸ find

$$\langle F_{14}^{B,+} | \hat{V} | CT_{11}^B \rangle = \frac{1}{2\sqrt{2}} (f_{n4'm1'} + f_{n4m1} + f_{m4'n1'} + f_{m4n1}) \quad (3.11)$$

where $f_{nimj} = (ni|\hat{f}|mj)$ is an element of the dimer Fock matrix, which is off-diagonal due to the perturbation, and we use the standard notation for a one-electron integral involving spatial orbitals.¹¹⁸

However, the Coulson-Rushbrooke theorem and the definition of the sign of monomer orbitals (see above) means that $f_{n4'm1'} = f_{n4m1}$ and $f_{m4'n1'} = f_{m4n1}$. We also find from the C_2 symmetry of the dimer that $f_{n4'm1'} = f_{m4'n1'}$ and $f_{n4m1} = f_{m4n1}$. These results simplify Eq. (3.11) to

$$\langle F_{14}^{B,+} | \hat{V} | CT_{11}^B \rangle = \sqrt{2} f_{n1m4}. \quad (3.12)$$

Expanding the monomer orbitals as $\phi_{ni} = \sum_{\lambda} c_{ni,\lambda} \chi_{\lambda}$ where χ_{λ} is a p orbital on atom λ , we find that all two-electron terms in Eq. (3.12) vanish within the neglect of differential overlap (NDO) assumption in PPP theory, leading to

$$\langle F_{14}^{B,+} | \hat{V} | CT_{11}^B \rangle = \sqrt{2} t c_{n1,\nu^*} c_{m4,\sigma^*} \quad (3.13)$$

where the monomers are connected through atom ν^* on monomer n and σ^* on monomer m , and t is the 'hopping' (resonance) term between atoms ν and σ , which is proportional to $\cos(\theta)$ where θ is the dihedral angle between the two monomers. Using intensity borrowing perturbation theory,¹²² we find that the dipole moment of the CT excitation is, to first order,

$$\langle \Phi_0 | \hat{\mu} | CT_{11}^{B,(1)} \rangle \simeq \langle \Phi_0 | \hat{\mu} | F_{14}^{B,+} \rangle \frac{\sqrt{2} t c_{n1,\nu^*} c_{m4,\sigma^*}}{E(CT_{11}^B) - E(F_{14}^{B,+})}. \quad (3.14)$$

and the intensity of the new absorption will be proportional to the square of the dipole moment.¹²⁰ We note that $\langle F_{14}^{A,+} | \hat{V} | CT_{11}^A \rangle = 0$ such that intensity can only be borrowed by the B CT excitation.

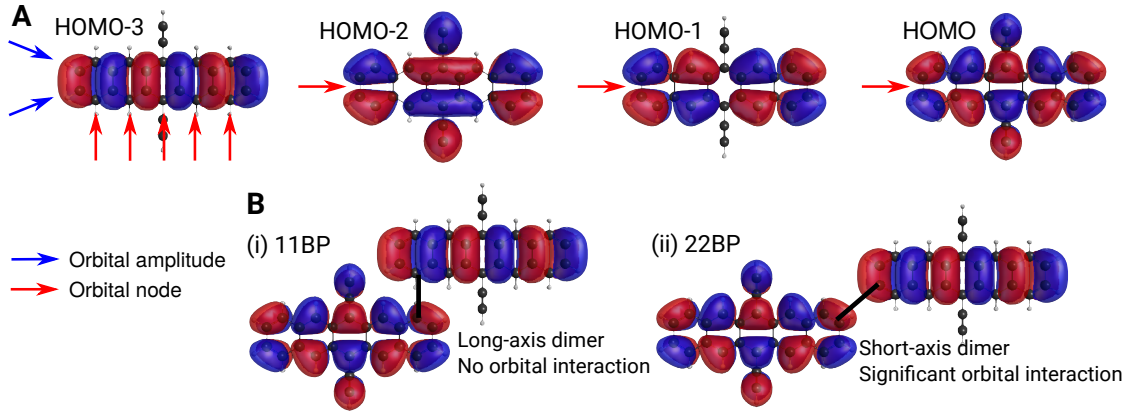


Figure 3.3: **A** Top four HOMOs of TIPS-pentacene. Transitions from the HOMO-3 contribute to the intense UV absorption in the monomer and those from the HOMO to a low-energy CT state. **B** shows how examining nodal structure of orbitals can explain the emergence of an extra absorption. Bonding along a long-axis carbon as for 11BP in **B**(i) leads to no significant interaction between the HOMO-3 on one monomer and the HOMO on the other. Conversely, bonding via a short-axis carbon as for 22BP in **B**(ii) leads to a significant orbital interaction. For clarity the dimers are drawn planar and with an elongated inter-monomer bond (thick black line) and long/short axes are defined in Fig. 3.1A.

3.3.2 Numerical Results

We calculate the relevant energies and orbitals (Fig. 3.3A) needed to evaluate the preceding equations for 22BP and find

$$\sqrt{2}t_0 \cos(\theta)c_{n1,\nu^*=2}c_{m4,\sigma^*=2} = 0.0860 \text{ eV} \quad (3.15)$$

$$E(\text{CT}_B) = 3.58 \text{ eV} \quad (3.16)$$

$$E(F_B) = 3.86 \text{ eV} \quad (3.17)$$

where we use the atom numbering in Fig. 3.1, such that

$$\frac{\langle F_{14}^{B,+} | \hat{V} | \text{CT}_{11}^B \rangle}{E(\text{CT}_{11}^B) - E(F_{14}^{+,B})} = -0.30. \quad (3.18)$$

The perturbation therefore corresponds to $(-0.30)^2 \approx 9\%$ of the UV peak intensity being borrowed. We stress that the result of 9% intensity borrowing is

only qualitative, since in practice there may be second-order contributions and mixing with other states. We can also qualitatively infer the strength of the perturbation from the relative magnitude of the new absorption around 500 nm in 22BP and the decrease in magnitude of the UV absorption from TIPS-pentacene. We observe that, while the new absorption dramatically changes the absorption in the visible (and the color of the molecule), the UV absorption in 22BP and 22eBP is still substantially more intense than the absorption around 500 nm, suggesting that the perturbation, while significant, is weak.

We can also approximately predict the energy of the low-energy absorption. The first order correction to the energy of the CT state is $\langle \text{CT}_B | \hat{V} | \text{CT}_B \rangle = -(n1n1|m1'm1') = -0.91$ eV, corresponding to the Coulomb attraction of an electron in the LUMO of one molecule and a hole in the HOMO of the other. This gives $E_{\text{CT}_B}^{(1)} = 2.67$ eV (464 nm), close to the experimentally observed transition at 496 nm.

The dihedral angle arguments advanced earlier for the strength of the absorption can also explain the more intense absorption seen in 22eBP. Considering the alkene linker to be a molecular ‘wire’ through which the monomers can interact, one would expect 22eBP to have a new absorption which is $\cos^2(0^\circ)/\cos^2(37^\circ) \approx 1.57$ times greater than the absorption in 22BP, which is approximately seen in the experimental spectra of Fig. 3.2A.

We now consider joining the two monomers at 1, 1' as opposed to the 2, 2' positions, shown schematically in Fig. 3.3B. For 11BP, we see that the HOMO has nonzero amplitude at the 1 position, but the HOMO-3 has zero amplitude due to its nodal structure. Consequently $c_{m4,\sigma^*} = 0$ in Eq. (3.14), $\langle \Phi_0 | \hat{\mu} | \text{CT}_{11}^{B,(1)} \rangle = 0$ and there is no new low-energy absorption.

To confirm the explanation for 11BP's missing peak, we also consider a near planar 6,6'-bipentacene (66yBP) as pictured in Figure 3.4A. The monomer units in 11BP are nearly orthogonal to one another, such that a purely dihedral angle argument could be made. However, for the planar 66yBP we also find no second peak in the experimental and PPP predicted spectrum, attributed to the same orbital coefficient reasoning. This confirms the importance of orbital structure for the prediction of observable intensity borrowing in these systems.

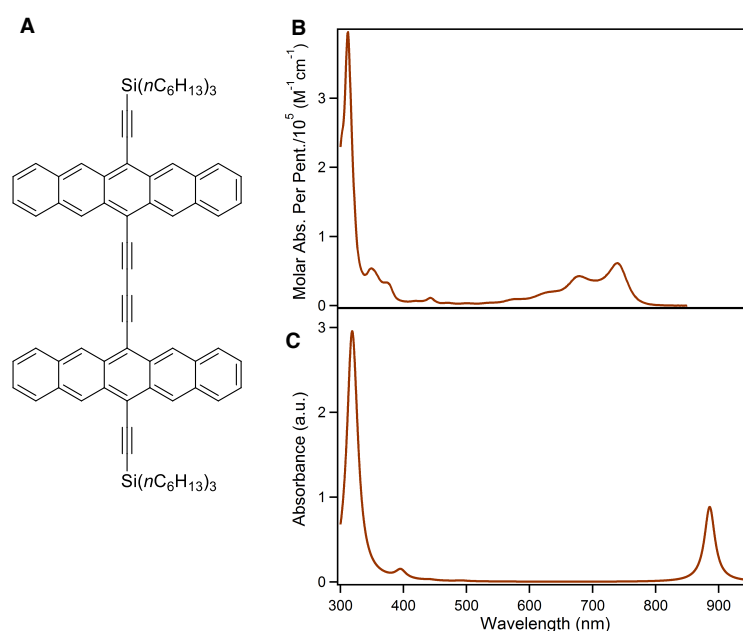


Figure 3.4: A) Structure of 66yBP. B) Experimental spectrum showing no second low-energy peak. C) PPP predicted spectrum confirming the absence of the second peak.

3.4 Design Principle

The above analysis leads us to the simple design principle that one must join the dimers along the short-axis carbons for intensity borrowing to occur and thus giving rise to a second peak in the visible. Furthermore, one may suggest

joining the acenes by *both* short-axis carbons, but the striped, HOMO-3 orbital of TIPS-pentacene has no xz node whereas the HOMO does, meaning that if there exists a long-axis symmetry plane through adjacent monomers there will be no net mixing and no intensity borrowing. This leads to an overall simple design rule:

For an extra low-energy absorption, join monomers via a short-axis carbon and avoid a long-axis symmetry plane passing through adjacent monomers.

and which is summarized in Fig. 3.5. Clearly, for the low-energy absorption to be significant, the π systems of the two monomers must be able to interact significantly; either the monomers must be directly bonded, otherwise held very close to each other, or connected via a conjugated linker (such as 22eBP). Similarly, we can also predict that planarity (low θ) is desirable for increasing the intensity of an extra absorption, but only if the design rule is already satisfied.

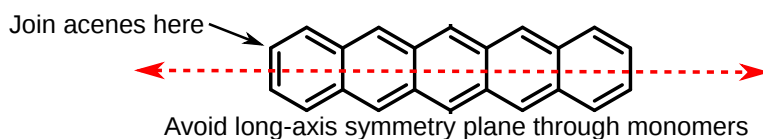


Figure 3.5: Design rule for an extra low-energy absorption in acene derivatives.

3.4.1 Range of Applicability

This rule makes an experimentally testable prediction. We therefore search the literature for acene dimers, trimers, oligomers and polymers and corresponding heteroatom-substituted derivatives which have been experimentally syn-

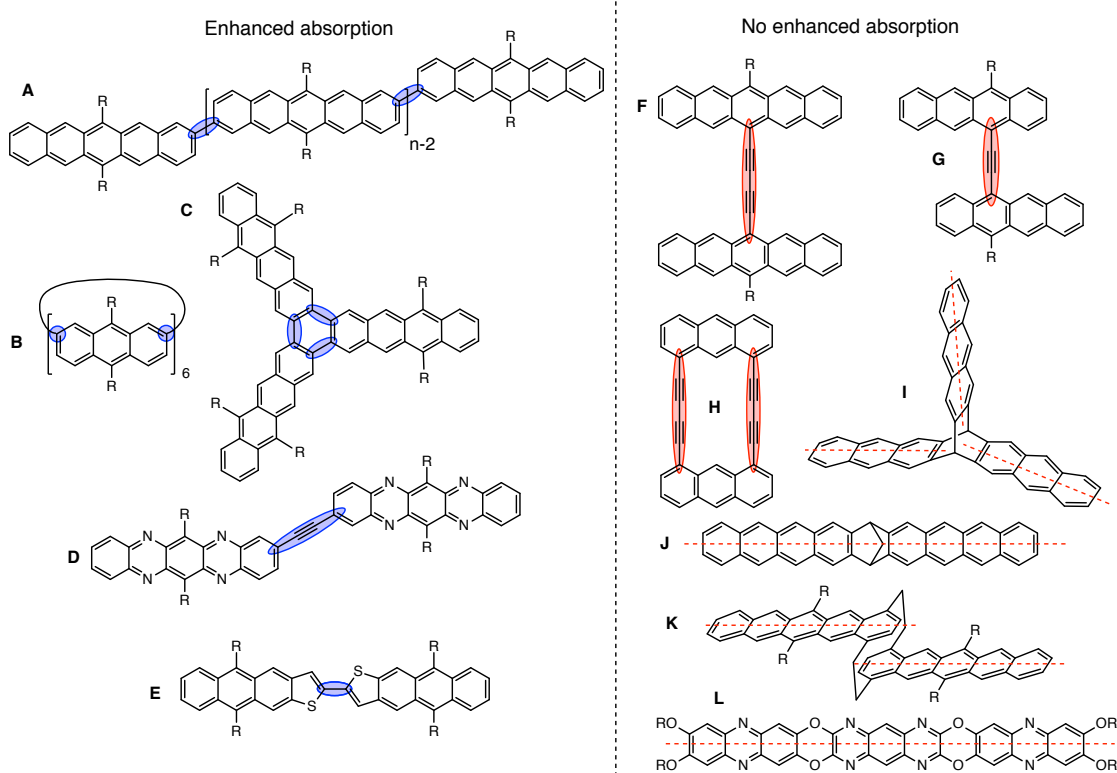


Figure 3.6: Illustrative examples of acene derivatives, showing how in every case the design rule correctly predicts the presence of absence of extra absorption. Left: molecules bonded via a short-axis carbon (blue oval) and without a horizontal (xz) symmetry plane through adjacent monomers, all of which show enhanced low-energy absorption in their experimental UV-vis spectra. Right: molecules bonded via a long-axis carbon (red oval), or such that the horizontal symmetry plane is preserved through adjacent monomers (red dashes), none of which show enhanced absorption compared to their corresponding monomer(s). The design principle correctly applies to acene dimers, oligomers and polymers such as **A**,¹¹ **B**,¹² **F**,¹³ **G**,¹⁴ and **H**,¹⁵ complex geometries such as **C**,¹⁶ **I**,^{17,18} **J**¹⁹ and **K**,²⁰ and to heteroatom-substituted dimers **D**,²¹ **E**,²² and **L**.²³ R denotes a solubilizing or stabilizing group.

thesized, and for which UV-vis spectra exist for both the oligomer and corresponding monomer(s).^{1,2,11–23,42,93,96}

A small selection of these are drawn in Fig. 3.6 grouped according to whether or not their spectra have enhanced low-energy absorption compared to their corresponding monomers. These molecules were created for a wide variety

of purposes including as a demonstration of organic synthesis,^{12,15,16,20} for organic semiconductors,^{13,21,22} liquid crystals,¹⁷ polymer synthesis,¹⁸ sensors,²³ photovoltaic applications,^{11,14,19} and one to explore structure-spectrum relationships.⁹⁶ Despite the wide variety of seemingly unrelated structures, the design principle correctly predicts the presence or absence of an extra absorption in all cases, including dimers, oligomers and polymers of naphthalene,⁹⁶ anthracene (Fig. 3.6B and Fig. 3.6H^{12,15}), tetracene (Fig. 3.6G¹⁴) and pentacene (Fig. 1, Fig. 3.6A and Fig. 3.6F^{1,11,13,42}), thereby explaining the structure-spectrum phenomenon first observed in 1948.⁹⁶ It also correctly predicts the presence or absence of an extra absorption for unusual and complex geometries such as starphenes (Fig. 3.6C¹⁶), iptycenes (Fig. 3.6I^{17,18}), bridged dimers (Fig. 3.6J¹⁹), and cyclophanes (Fig. 3.6K²⁰).

Perhaps surprisingly, the design rule also holds in heteroatom-substituted acene derivatives such as the tetra-aza-pentacene dimer in Fig. 3.6D,²¹ the anthrathiophene dimer in Fig. 3.6E²² and the aza-anthracene trimer Fig. 3.6L²³ (compared to its corresponding monomers^{123,124}). This unexpected applicability probably occurs since the ‘striped’ orbitals in Fig. 3.3A will be solutions to the Hückel Hamiltonian of the heteroatom-substituted acene provided that only the diagonal energies (ϵ_μ in Eq. (3.1)) are perturbed and not the off-diagonal ($t_{\mu\nu}$) terms, and that the heterosubstitution is only on long-axis carbons. This explains the applicability to aza-substituted derivatives in Fig. 3.6D and L. For the thiophene derivative, standard organic chemistry¹²⁵ suggests that the S heteroatom is of a similar size to a C=C double bond, and therefore thiophene qualitatively similar to benzene. With this reasoning the anthrathiophene dimer can be likened to a 2, 2'-tetracene dimer, explaining the new low-energy absorption.

Finally, we note that application of the design rule is perhaps unclear for cases where two or more moieties overlap in such a way that through-space interaction becomes important, such as the cross-conjugated dimers in Refs 37, 126. In these cases PPP theory cannot capture the proper interactions in the hopping term alone and our intensity borrowing analysis will not be valid.

3.5 Summary

Taken together, this chapter shows how application of intensity borrowing perturbation theory leads to a simple rule for predicting and explaining the low-energy absorption spectra of acene derivatives. This testable and experimentally verifiable design rule has been found to hold in a large variety of dimers, trimers, oligomers and polymers, including those with heteroatom substitution and unusual bonding geometries.

The *a priori* design of highly absorbent molecules, of which this is a proof-of-concept, has significant implications for photovoltaic design, where some organic solar photovoltaics are constrained by the small diffusion length of excitons compared to the thickness of material required to absorb a significant fraction of visible light.⁹⁷ Developing more absorbent molecules which retain the necessary photophysical charge-transport properties could allow for thinner, flexible, cheaper and more efficient solar cells.

CHAPTER 4

NONADIABATIC RELAXATION AT METAL SURFACES

Understanding gas phase reactions at metal surfaces is crucial for the development of novel catalysis and sensor technologies. Therefore, one hopes to construct models with predictive capabilities of properties such as diffusion timescales, sticking probabilities, and binding energies. However, it is unclear if one of the most common approximations made in quantum chemical models, the Born-Oppenheimer approximation, is valid for such systems.

Recently, many excellent experiments seem to demonstrate an underlying nonadiabatic mechanism in the scattering of diatoms (NO,CO,N₂) from metal surfaces (Au,Ag,Pt).¹²⁷⁻¹²⁹ In particular, it has been observed that many quanta of vibrational energy can be transferred from the diatom to the metal. This process appears to be dependent on the initial vibrational state of the diatom and its initial translational energy (and surface temperature of the metal), with a threshold for nonadiabatic activity. Below this threshold the diatom will simply scatter from the surface and return to the detector in a vibrational state near the one in which it was prepared, while above the threshold a distribution of multiquanta relaxed vibrational states will be observed. Wodtke and coworkers point to this feature as evidence of a distinctly nonadiabatic mechanism.¹³⁰

4.1 Qualitative Mechanism

Qualitatively the mechanism behind the observed scattering trends is believed to be known — near the surface, charge transfer from the metal to the diatom

can occur, forming a transient negatively charged species. As the diatom scatters away from the surface, back electron transfer occurs with concomitant energy transfer, resulting in the observation of relaxed vibrational states. In order for the transient anion to be formed, the diatom must access anionically favored regions of the PES. Clearly the initial translational energy plays a role in determining what regions of the PES will be explored. It is expected that as an anion approaches the surface an image charge stabilization¹³¹ will help lower its energy relative to a neutral species. Furthermore, the anion will be stabilized when the diatom is in a vibrationally excited state, as stretched geometries result in greater electron affinities.

The above considerations suggest that it will once again be beneficial to analyze our problem from a diabatic standpoint — neutral and anionic diatomic diabats. This idea was adopted in some of the first explicit dynamic simulations of these types of scattering events.^{132,133} Despite apparent initial successes,^{134,135} these models cannot accurately reproduce the observed scattering trends across all experimental regimes.¹²⁸ The limitations of these simulations stem from inaccurate PES, inaccurate approximate dynamics, or a combination of both.¹²⁷

4.2 Model Details

We would like to create a physically accurate model for these gas phase scattering events, here we focus on the specific case of NO scattering from a Au(111) surface. To allow for intuitive interpretation of results and transferability to other systems, we seek a simple model that still retains the essential physics of the problem. Furthermore, we are interested in calculating localized diabatic

states with the characteristics of neutral and anionic NO, respectively. We will discuss our progress made on this front by detailing the model Hamiltonian used and the technique employed to create intuitive localized diabatic states.

4.2.1 Newns Hamiltonian

The Hamiltonian describing the ground state NO-Au(111) potential energy surface (Eq. 4.1) is constructed from three main components: a Newns Hamiltonian¹³⁶ describing the NO-Au(111) electronic interactions, a previously described full PES for free NO,¹³⁷ and a NO-Au(111) nuclear repulsion term.

$$H_{tot} = H_{Newns} + H_{NO} + H_{nuc} \quad (4.1)$$

The Newns Hamiltonian (Eq. 4.2) itself is comprised of three terms.

$$H_{Newns}(\mathbf{r}, \mathbf{Z}) = \epsilon(\mathbf{r}, \mathbf{Z})c^\dagger c + \sum_k \epsilon_k c_k^\dagger c_k + t(\mathbf{Z}) \sum_k (c^\dagger c_k + c_k^\dagger c) \quad (4.2)$$

The first describes the effective orbital energy of the approaching NO. ϵ is constructed according to Eq. 4.3 where the work function (WF) of Au(111) is taken to be 5.31 eV,¹³⁸ the vertical electron affinity is calculated from the potential energy surfaces reported in ref. 137, and the form of the final term (the image charge stabilization) is adopted from a previous study,¹³⁹ where the location of the image plane (Z_i) is set to 1.15 .

$$\epsilon = WF - E_{ea}(r) - \frac{1 - e^{-1.25(Z_{coc} - Z_i)}}{4(Z_{coc} - Z_i)} \quad (4.3)$$

Z_{coc} is the position of the center of charge of the NO molecule defined using the electronegativities of both atoms as

$$Z_{coc} = Z \frac{\chi_O}{\chi_N + \chi_O} + (Z + r) \frac{\chi_N}{\chi_N + \chi_O}. \quad (4.4)$$

The continuum of ϵ_k 's are discretized¹⁴⁰ with a bandwidth of 7 eV¹⁴¹ centered about the Fermi level. Finally, the NO-Au(111) coupling (Eq. 4.5) is described in a manner similar to the falloff of the overlap between Slater-type orbitals.¹⁴²

$$t = t_0 e^{-0.2Z} \quad (4.5)$$

We note that t_0 is our one completely free parameter. For the proceeding analysis we set it to a physically reasonable value of 5.0 eV. One could perhaps find this value from the splitting of the local density of states found from an *ab initio* calculation. However, the accuracy of a calculation like this is questionable so we instead choose to work with an easily tunable parameter. To account for the missing nuclear information in the Newns Hamiltonian, a screened Thomas-Fermi potential (Eq. 4.6) is used.

$$H_{nuc} = \frac{A}{Z} e^{-BZ} \quad (4.6)$$

A and B are parameters used to reproduce the expected equilibrium NO-Au(111) distance and energy.¹⁴³

The total Hamiltonian is therefore a function of two nuclear degrees of freedom: N-O bond distance (r) and metal-N distance (Z). Thus we can create a 2-D PES by scanning the two dimensions, forming the Hamiltonian, and diagonalizing it to find the ground state wavefunction and energy.

4.2.2 Construction of Diabatic Surfaces

Following the construction of the ground state wavefunction (here, a single Slater determinant), we would like to form localized diabatic-like states to allow for easier interpretation of results, much like our work on singlet fission. We

do so by utilizing the Schmidt decomposition (SD) of the ground state wavefunction. The SD has become a useful tool in quantum information theory to describe the entanglement between a subsystem and its surroundings.¹⁴⁴ In the context of quantum chemistry, the SD is an essential element to the density matrix renormalization group and density matrix embedding theory (DMET).^{145,146} The SD allows for the identification of the most important states which should be included in a calculation.

In our case the wavefunction is partitioned into system+bath (Eq. 4.7) where the NO orbital is treated as the system,

$$|\Psi\rangle = \sum_{i=1}^n \tilde{\chi}_i |S_i\rangle |B_i\rangle \quad (4.7)$$

where $n = \min(\dim(H_S), \dim(H_B))$. Because the dimensionality of our system is one, this results in the identification of a *single* effective metal “bath” orbital, which describes the NO-Au(111) entanglement in its entirety, and unentangled metal core orbitals. Charge transfer from the metal surface to the NO takes place via the effective bath orbital, enabling intuitive diabatic states to be defined. These states (neutral/anionic) are constructed from Slater determinants by occupying the core and bath/NO orbitals according to Eq. 4.8.

$$|\psi_n\rangle = |\text{core}, \text{bath}\rangle, |\psi_a\rangle = |\text{core}, \text{NO}\rangle \quad (4.8)$$

The off-diagonal coupling, $\langle \psi_n | \hat{H} | \psi_a \rangle$, is found following the Slater-Condon rules.¹⁴⁷

In practice the SD is performed following Ref. 148. We first form the density matrix defined by Eq. 4.9, where the C 's are orbital coefficients and the sum goes over all occupied orbitals.

$$D_{\mu\nu} = \sum_a^N C_{\mu a} C_{\nu a}^* \quad (4.9)$$

Typically, it would be necessary to perform an orbital localization prior to the formation of the density matrix, so that the system of interest could more readily be assigned. However, because the Newns Hamiltonian is represented in a local 'site' basis from the beginning, we can unequivocally assign blocks of the density matrix as (system \times system), (environment \times environment), and mixed (system \times environment).

Once the environment subblock has been identified it can be diagonalized to produce its eigenvalues and eigenvectors. Because the overall density matrix is idempotent (it is produced from a single Slater determinant), all of the eigenvalues associated with the environment subblock will lie between 0 and 1. In fact, only $m=\text{dim}(\text{system})$ eigenvalues will not be exactly 1¹⁴⁹—the eigenvectors corresponding to these eigenvectors are the entangled bath orbitals. All other eigenvectors represent unentangled core orbitals.

Finally, we note that the states formed via the SD are not produced via an explicit diabaticization procedure like was used for our description of SF-adiabatic states have not been directly rotated into this basis via a transformation. Instead, we work directly with individual CSF's. The two localized states, and their coupling are plotted in Figure 4.1.

4.3 Exact Quantum Dynamics

In order to probe for the nonadiabatic behavior that has been observed experimentally, we would now like to perform dynamics simulations using the surfaces generated in the last section (fits to analytic functions are given in Appendix C). One particularly well suited approach for accomplishing this would

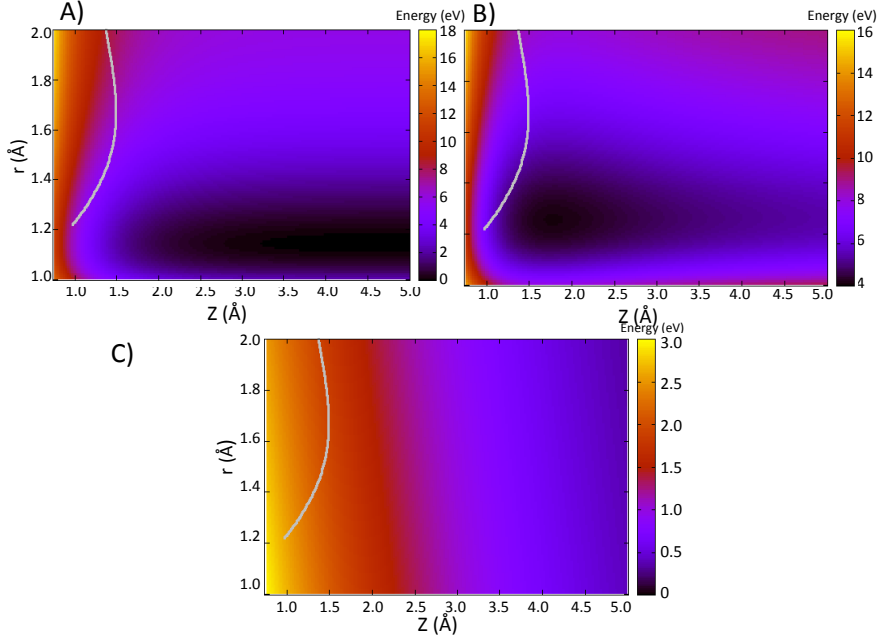


Figure 4.1: A) The neutral diabatic state of the NO-metal surface system. B) The anionic diabatic state of the NO-metal surface. A clear local minimum is present $\sim(1.75,1.20)$. C) The coupling between diabatic surfaces. In all plots the gray curve marks the points at which the two states become degenerate.

be approximate nonadiabatic semiclassical methods.^{150,151} However, because the dimensionality of our problem is small, it is possible to perform exact quantum dynamics. We accomplish this through a discrete variable representation (DVR) of the Hamiltonian. In particular, we employ a grid sinc basis¹⁵² such that the kinetic energy matrix elements can be evaluated as

$$T_{nn',ii',jj'} = \delta_{nn'}(T_{ii'} + T_{jj'}) \quad (4.10)$$

$$T_{ii'} = \delta_{jj'} \frac{\hbar^2}{2m_1 \Delta r^2} (-1)^{i-i'} \begin{cases} \pi^3/3, & i = i' \\ \frac{2}{(i-i')^2}, & i \neq i' \end{cases} \quad (4.11)$$

$T_{jj'}$ is similarly defined where n labels the electronic states, i the grid points in the r dimension, and j the grid points in the Z dimension. The potential matrix

elements are evaluated as

$$V_{mm',ii',jj'} = \delta_{ii'}\delta_{jj'}V_{mm'}(r[i],Z[j]) \quad (4.12)$$

We discretize Z in the range [1:5] Å in steps of 0.05 Å, while for r we use a range of [0.5:2] Å in steps of 0.02 Å. In order to simplify the formation of the exact propagator, we truncate the number of calculated eigenvalues/eigenvectors of our DVR Hamiltonian. This step helps to drastically decrease the dimensionality, ensuring tractability. We take care to include enough states such that the norm of the wavefunction is >99% preserved throughout the simulation. The initial wavefunction is formed as a product of an r -dependent function and a Z -dependent function. The r component is initialized in a particular vibrational state found via diagonalization of the ground state NO Hamiltonian using the appropriate Morse potential, while the Z component is initialized as a Gaussian wavepacket in the form,

$$\phi(Z) = \frac{1}{\sqrt[4]{\sigma^2\pi}} e^{-(Z-Z_0)^2/2\sigma^2} e^{ip_0/\hbar(Z-Z_0)} \quad (4.13)$$

where σ is set to 0.25 \AA^{-1} , Z_0 is the initial placement of the wavepacket and p_0 is set to correspond to experimental initial translational energy.

4.3.1 Results

Figure 4.2 shows $|\phi|^2$ along a typical scattering trajectory. With a low initial translational energy, the NO does not penetrate close to the surface where the two diabats become similar in energy. As a consequence, little population is transferred from the neutral diabat to the anionic diabat. This can be seen in Fig. 4.3, which also displays $\langle Z \rangle(t)$ and $\langle r \rangle(t)$ for different wavefunction initializations.

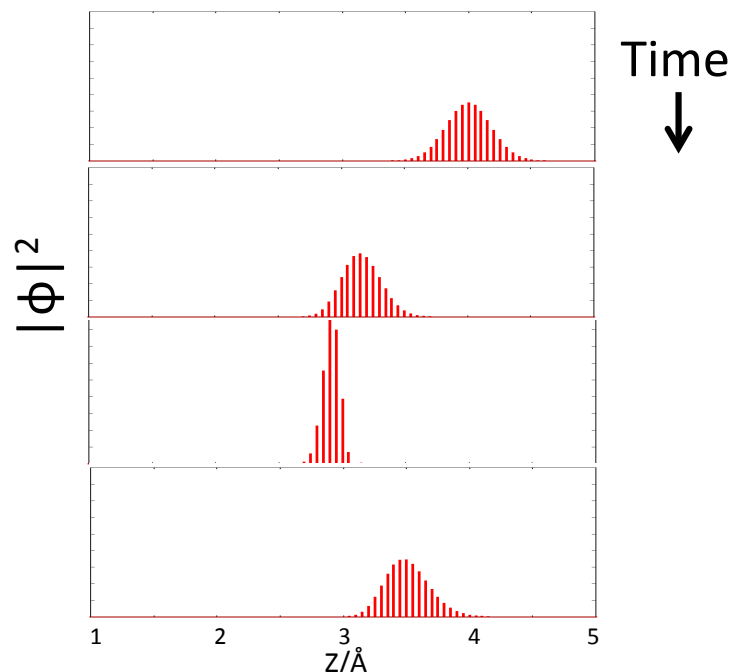


Figure 4.2: $|\phi|^2$ projected onto the metal-N coordinate (Z) for a simulation with $E_i=0.1$ eV and $\nu_i=3$. Simulation time increases down the figure. The wavefunction reflects from the surface potential at $Z \approx 2.5$ Å.

Population transfer can be enhanced by increasing the initial NO vibrational state, the incident kinetic energy, or both. This observation is in line with physical expectations.

It is interesting to note that $\langle r \rangle$ (Fig. 4.3C) does not decrease at long time which may be expected if ν is smaller. At intermediate and long times $\langle r \rangle$ rapidly oscillates due to the vibrational state falling from its initially prepared eigenstate. The oscillations possess larger amplitudes when starting in $\nu_i=15$ as compared to a lower vibrational state. This is evidence of increased nonadiabatic behavior. More simulations are needed to understand this nonadiabaticity as a whole. In particular, examining $|\nu_j\rangle\langle\nu_j|$ as a function of time may reveal a clearer picture of the process.

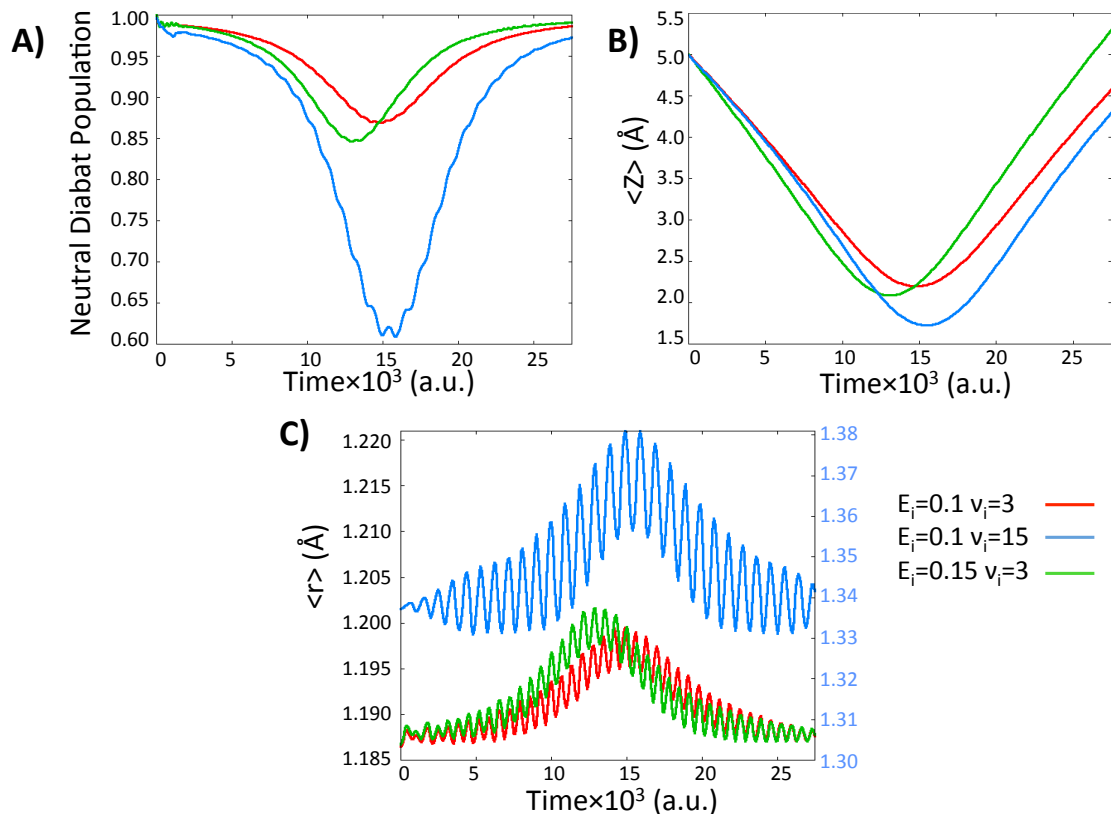


Figure 4.3: Expectation values of the neutral state population (A), metal-N (Z) distance (B), and N-O (r) distance (C) for three different combinations of initial translational energy (E_i) and initial vibrational states (ν_i) ($E_i=0.1$ eV, $\nu_i=3$ (red), $E_i=0.1$ eV, $\nu_i=15$ (blue), $E_i=0.2$ eV, $\nu_i=3$ (green)).

4.4 Summary and Future Work

We have detailed a model for describing the interactions of an adsorbate with a metal surface based upon the Newns Hamiltonian. Through the novel use of a Schmidt decomposition, we have shown how intuitive diabatic-like states can be formed, allowing for approximate or exact quantum dynamic calculations. Preliminary dynamics calculations agree with qualitative expectations, showing increased nonadiabatic behavior at higher initial kinetic energy and vibrational states.

More simulations across wider initial conditions are needed, however, to determine the robustness of our model. In particular, altering our one free parameter, the coupling term t_0 , will allow us to explore different interaction regimes. Furthermore, it may be necessary to include bath degrees of freedom such that energy can be dissipated from the adsorbate degrees of freedom, so that inelastic scattering can occur. Finally, it would be interesting to test the applicability of the Schmidt decomposition prescription for the creation of diabatic states in other contexts. Since the wavefunction is still a single Slater determinant, it may be useful in DFT applications as an alternative to constrained-DFT.¹⁵³

CHAPTER 5

CONCLUSIONS AND FUTURE DIRECTIONS

This dissertation has focused on the quantum mechanical investigations of nonadiabatic systems. In each study discussed here we have found it useful to take a local, pseudo-diabatic view of the problem. This has allowed for chemically meaningful and intuitive analyses with the goal of understanding processes relevant to photovoltaics, catalysis, and other novel technologies.

We first discussed intramolecular singlet fission in bipentacenes. Representing the excited states in terms of diabatic configurations, we showed that charge transfer states are far removed from other low-lying states. However, due to a quasi-degeneracy between local excitonic states and the multiexcitonic state, weak direct coupling is able to explain the ultrafast timescale of SF. This direct mechanism is facilitated by a ring-breathing vibrational mode. Quantum dynamics simulations supported this mechanism, predicting SF on experimental timescales.

In Chapter 3 our investigation of bipentacenes led us to examine the steady-state spectra of a variety of dimers differing in bonding topology. A home-built PPP theory code was written and used to accurately reproduce spectra. The simple and intuitive structure of the PPP Hamiltonian was exploited in perturbative intensity borrowing calculations, which led us to develop a straightforward explanation for the appearance of a second low energy peak in the spectra of oligoacenes. We showed the applicability of this rule to an enormous variety of compounds, with the hope that more intensely absorbent chromophores can be intelligently designed.

In Chapter 4 we detailed a model for the scattering of diatoms from metal surfaces. Invoking a Newns Hamiltonian, we were able to retain the essential physics of the situation, while allowing for a natural interpretation of results. Once again, we viewed the problem with a sense of locality, forming diabatic-like states through a novel application of the Schmidt decomposition. Via the Schmidt decomposition, we were able to form surfaces on which to perform exact quantum dynamics using the discrete variable representation. Preliminary dynamics simulations agreed with expectations and previous results, but further tests are needed to provide a full description of the nonadiabatic process.

In the context of iSF, it will be interesting to apply similar analyses to the problem of triplet-triplet recombination. Recombination appears to be the primary loss pathway for excitons generated via SF and as such a detailed understanding of the process is needed. It is not yet clear if triplets recombine to form the ground singlet state or an excited state. Regardless of the dominant relaxation product, it may be possible to engineer a chromophore in which the multiexcitonic triplets do not interact with one another once they are formed. This may be accomplished through intermonomer geometric rearrangements unique to the multiexcitonic state. In particular, using butadiene as a possible linker may provide such rearrangements, as it is known that its $2A_g$ state is highly twisted compared to its $1A_g$ and $1B_u$ states.¹⁵⁴

Finally, it may be intriguing to investigate novel applications of the Schmidt decomposition. In particular, ideas used in the identification of effective "bath" orbitals may prove useful when applied to methods using a reduced description of the wavefunction such as natural orbital theories, or 2-RDM theories.^{155,156} Applying a similar methodology for the construction of diabatic-like states to

a DFT wavefunction may yield robust and chemically intuitive states similar to those produced using constrained-DFT.¹⁵³ For this application a localization procedure would be required, making the process more difficult than the one described here. However, localization is common in constrained-DFT methods as well and so the SD method may overall be simpler to perform. If this is the case, accurate and meaningful diabatic states can be produced for systems with increased size, such that large-scale nonadiabatic processes can be investigated.

APPENDIX A
MOLECULAR COORDINATES

Coordinates For The Reference Structure Of 22BP.

C -6.55539 1.18082 -0.38359
C -7.04107 -1.53091 0.38844
C -6.31367 2.53042 -0.76782
C -7.28280 -2.88052 0.77266
C -6.10780 3.67983 -1.09506
C -7.48866 -4.02994 1.09989
H -5.92675 4.69068 -1.38284
H -7.66970 -5.04077 1.38768
C -7.88553 0.67453 -0.38910
C -5.46434 0.35220 0.00197
C -8.13211 -0.70230 0.00287
C -5.71095 -1.02461 0.39395
C -8.98354 1.47780 -0.76775
C -4.13642 0.83254 0.01517
C -9.46005 -1.18262 -0.01032
C -4.61290 -1.82789 0.77259
H -8.79699 2.50669 -1.06040
H -3.95431 1.86204 -0.27819
H -9.64214 -2.21212 0.28305
H -4.79948 -2.85678 1.06524
C -10.28708 0.99339 -0.77675
C -3.06308 0.03172 0.39008

C -10.53338 -0.38180 -0.38524
C -3.30938 -1.34347 0.78158
C -11.40416 1.80786 -1.16112
C -1.71306 0.51776 0.40421
C -11.88339 -0.86786 -0.39937
C -2.19231 -2.15794 1.16598
H -11.21621 2.83829 -1.45409
H -1.53172 1.54908 0.11018
H -12.06474 -1.89917 -0.10534
H -2.38024 -3.18838 1.45893
C -12.67428 1.30248 -1.15966
C -0.67893 -0.29436 0.77783
C -12.91752 -0.05573 -0.77299
C -0.92220 -1.65256 1.16453
H -13.51251 1.92907 -1.45283
H -13.93596 -0.43516 -0.77973
H -0.08395 -2.27915 1.45767
C 6.55538 -1.18081 -0.38359
C 7.04107 1.53090 0.38844
C 6.31367 -2.53042 -0.76781
C 7.28280 2.88052 0.77266
C 6.10780 -3.67984 -1.09506
C 7.48866 4.02994 1.09989
H 5.92675 -4.69069 -1.38284
H 7.66971 5.04078 1.38768
C 7.88552 -0.67453 -0.38910

C 5.46434 -0.35221 0.00197
C 8.13211 0.70231 0.00287
C 5.71094 1.02461 0.39395
C 8.98354 -1.47780 -0.76775
C 4.13642 -0.83255 0.01517
C 9.46005 1.18263 -0.01033
C 4.61290 1.82789 0.77259
H 8.79699 -2.50670 -1.06040
H 3.95431 -1.86203 -0.27819
H 9.64214 2.21212 0.28305
H 4.79948 2.85679 1.06524
C 10.28708 -0.99339 -0.77675
C 3.06308 -0.03172 0.39008
C 10.53338 0.38180 -0.38524
C 3.30939 1.34347 0.78158
C 11.40417 -1.80787 -1.16112
C 1.71306 -0.51776 0.40420
C 11.88340 0.86786 -0.39937
C 2.19231 2.15795 1.16597
H 11.21622 -2.83830 -1.45409
H 1.53172 -1.54909 0.11018
H 12.06474 1.89918 -0.10534
H 2.38024 3.18839 1.45893
C 12.67427 -1.30248 -1.15966
C 0.67893 0.29436 0.77783
C 12.91752 0.05573 -0.77299

C 0.92220 1.65256 1.16453

H 13.51251 -1.92907 -1.45282

H 13.93596 0.43516 -0.77974

H 0.08395 2.27915 1.45767

Optimized S_1 Structure Of The Truncated TIPS-Pentacene Monomer.

C 0.00000000 1.42927015 0.00000000
C 0.00000000 -1.42927015 0.00000000
C 0.00000000 2.84705758 0.00000000
C 0.00000000 -2.84705758 0.00000000
C 0.00000000 4.06055307 0.00000000
C 0.00000000 -4.06055307 0.00000000
H 0.00000000 5.12811708 0.00000000
H 0.00000000 -5.12811708 0.00000000
C 1.24618638 0.72458410 0.00000000
C -1.24618638 0.72458410 0.00000000
C 1.24618638 -0.72458410 0.00000000
C -1.24618638 -0.72458410 0.00000000
C 2.47300339 1.39509976 0.00000000
C -2.47300339 1.39509976 0.00000000
C 2.47300339 -1.39509976 0.00000000
C -2.47300339 -1.39509976 0.00000000
H 2.47154498 2.48253703 0.00000000
H -2.47154498 2.48253703 0.00000000
H 2.47154498 -2.48253703 0.00000000
H -2.47154498 -2.48253703 0.00000000
C 3.71313381 0.71891922 0.00000000
C -3.71313381 0.71891922 0.00000000
C 3.71313381 -0.71891922 0.00000000
C -3.71313381 -0.71891922 0.00000000
C 4.95171928 1.40184164 0.00000000

C -4.95171928 1.40184164 0.00000000
C 4.95171928 -1.40184164 0.00000000
C -4.95171928 -1.40184164 0.00000000
H 4.94953203 2.49046826 0.00000000
H -4.94953203 2.49046826 0.00000000
H 4.94953203 -2.49046826 0.00000000
H -4.94953203 -2.49046826 0.00000000
C 6.14844370 0.70437098 0.00000000
C -6.14844370 0.70437098 0.00000000
C 6.14844370 -0.70437098 0.00000000
C -6.14844370 -0.70437098 0.00000000
H 7.09218216 1.24478328 0.00000000
H -7.09218216 1.24478328 0.00000000
H 7.09218216 -1.24478328 0.00000000
H -7.09218216 -1.24478328 0.00000000

Optimized T_1 Structure Of The Truncated TIPS-Pentacene Monomer.

C 0.00000000 1.43657625 0.00000000
C 0.00000000 -1.43657625 0.00000000
C 0.00000000 2.84920144 0.00000000
C 0.00000000 -2.84920144 0.00000000
C 0.00000000 4.06490421 0.00000000
C 0.00000000 -4.06490421 0.00000000
H 0.00000000 5.13127995 0.00000000
H 0.00000000 -5.13127995 0.00000000
C 1.25642908 0.72565770 0.00000000
C -1.25642908 0.72565770 0.00000000
C 1.25642908 -0.72565770 0.00000000
C -1.25642908 -0.72565770 0.00000000
C 2.47491884 1.39652407 0.00000000
C -2.47491884 1.39652407 0.00000000
C 2.47491884 -1.39652407 0.00000000
C -2.47491884 -1.39652407 0.00000000
H 2.47517848 2.48266292 0.00000000
H -2.47517848 2.48266292 0.00000000
H 2.47517848 -2.48266292 0.00000000
H -2.47517848 -2.48266292 0.00000000
C 3.72162890 0.71660829 0.00000000
C -3.72162890 0.71660829 0.00000000
C 3.72162890 -0.71660829 0.00000000
C -3.72162890 -0.71660829 0.00000000
C 4.95959187 1.40299916 0.00000000

C -4.95959187 1.40299916 0.00000000
C 4.95959187 -1.40299916 0.00000000
C -4.95959187 -1.40299916 0.00000000
H 4.95702934 2.49070835 0.00000000
H -4.95702934 2.49070835 0.00000000
H 4.95702934 -2.49070835 0.00000000
H -4.95702934 -2.49070835 0.00000000
C 6.15538931 0.70583850 0.00000000
C -6.15538931 0.70583850 0.00000000
C 6.15538931 -0.70583850 0.00000000
C -6.15538931 -0.70583850 0.00000000
H 7.09895086 1.24505115 0.00000000
H -7.09895086 1.24505115 0.00000000
H 7.09895086 -1.24505115 0.00000000
H -7.09895086 -1.24505115 0.00000000

12BP Structure Used for PPP Calculations

C -5.0168112146 1.6786790667 0.0464831369
C 5.0168112146 -1.6786790667 0.0464831369
C -3.7770489120 -0.8995243633 -0.0234142169
C 3.7770489120 0.8995243633 -0.0234142169
C -5.6341113352 2.9610319681 0.0836332259
C 5.6341113352 -2.9610319681 0.0836332259
C -3.1608849614 -2.1824592852 -0.0580493116
C 3.1608849614 2.1824592852 -0.0580493116
C -6.1618397466 4.0524937895 0.1147753046
C 6.1618397466 -4.0524937895 0.1147753046
C -2.6362554178 -3.2751541152 -0.0859442496
C 2.6362554178 3.2751541152 -0.0859442496
H -6.6270642889 5.0117618599 0.1402879113
H 6.6270642889 -5.0117618599 0.1402879113
H -2.1654838949 -4.2317995341 -0.1083126340
H 2.1654838949 4.2317995341 -0.1083126340
C -5.5622687669 0.6571259705 -0.7810752597
C 5.5622687669 -0.6571259705 -0.7810752597
C -3.8603762837 1.4291449469 0.8376328753
C 3.8603762837 -1.4291449469 0.8376328753
C -4.9366736721 -0.6530391474 -0.8115082957
C 4.9366736721 0.6530391474 -0.8115082957
C -3.2276382667 0.1245364571 0.7985422638
C 3.2276382667 -0.1245364571 0.7985422638
C -6.7048631222 0.8805966134 -1.5805194842

C 6.7048631222 -0.8805966134 -1.5805194842
C -3.2998609203 2.4214212570 1.6698352866
C 3.2998609203 -2.4214212570 1.6698352866
C -5.5017716946 -1.6548483714 -1.6313085290
C 5.5017716946 1.6548483714 -1.6313085290
C -2.0748711290 -0.0989087129 1.5847195629
C 2.0748711290 0.0989087129 1.5847195629
H -7.1682027183 1.8623796989 -1.5602718633
H 7.1682027183 -1.8623796989 -1.5602718633
H -3.7724288545 3.3985212045 1.7025429323
H 3.7724288545 -3.3985212045 1.7025429323
H -5.0342209852 -2.6346700386 -1.6485433777
H 5.0342209852 2.6346700386 -1.6485433777
H -1.6088469264 -1.0763983682 1.5451099309
H 1.6088469264 1.0763983682 1.5451099309
C -7.2493988858 -0.1126690066 -2.3876427575
C 7.2493988858 0.1126690066 -2.3876427575
C -2.1669125893 2.1903869510 2.4432341397
C 2.1669125893 -2.1903869510 2.4432341397
C -6.6303294657 -1.4242279454 -2.4106306834
C 6.6303294657 1.4242279454 -2.4106306834
C -1.5280677528 0.8865209381 2.4013913396
C 1.5280677528 -0.8865209381 2.4013913396
C -8.4084149891 0.1132809950 -3.2031695924
C 8.4084149891 -0.1132809950 -3.2031695924
C -1.6120311759 3.2120194516 3.2823688117

C 1.6120311759 -3.2120194516 3.2823688117
C -7.2071942329 -2.4409706094 -3.2433249054
C 7.2071942329 2.4409706094 -3.2433249054
C -0.3437935893 0.6649544380 3.2076966897
C 0.3437935893 -0.6649544380 3.2076966897
H -8.8683908544 1.0986165748 -3.1862532429
H 8.8683908544 -1.0986165748 -3.1862532429
H -2.1010646062 4.1830056111 3.3088108062
H 2.1010646062 -4.1830056111 3.3088108062
H -6.7426838926 -3.4242233517 -3.2556394540
H 6.7426838926 3.4242233517 -3.2556394540
C -8.9228223218 -0.8846949932 -3.9831660604
C 8.9228223218 0.8846949932 -3.9831660604
C -0.4946723195 2.9676969390 4.0285519904
C 0.4946723195 -2.9676969390 4.0285519904
C -8.3140535576 -2.1814329492 -4.0025104129
C 8.3140535576 2.1814329492 -4.0025104129
C 0.1409618000 1.6875984915 3.9854886973
C -0.1409618000 -1.6875984915 3.9854886973
H -9.8016592260 -0.7011761381 -4.5958530875
H 9.8016592260 0.7011761381 -4.5958530875
H -0.0768503612 3.7433357089 4.6650280256
H 0.0768503612 -3.7433357089 4.6650280256
H -8.7419485671 -2.9596339230 -4.6292654463
H 8.7419485671 2.9596339230 -4.6292654463
H 1.0306306985 1.5196266204 4.5868899340

H -1.0306306985 -1.5196266204 4.5868899340

22eBP Structure Used for PPP Calculations

C -7.92668247 -1.26516759 0.00000000
C 7.92667723 1.26516676 0.00000000
C -8.31315231 1.56966603 0.00000000
C 8.31314659 -1.56966686 0.00000000
C -7.73448944 -2.67577052 0.00000000
C 7.73448372 2.67576981 0.00000000
C -8.50554085 2.98072267 0.00000000
C 8.50553513 -2.98072338 0.00000000
C -7.57011127 -3.87732530 0.00000000
C 7.57005262 3.87731624 0.00000000
C -8.67098522 4.18200779 0.00000000
C 8.67100811 -4.18200445 0.00000000
H -7.42592239 -4.93404913 0.00000000
H 7.42644835 4.93412924 0.00000000
H -8.81589413 5.23868799 0.00000000
H 8.81561184 -5.23873091 0.00000000
C -9.24816132 -0.73380011 0.00000000
C 9.24815559 0.73379898 0.00000000
C -6.79677439 -0.40012172 0.00000000
C 6.79676867 0.40012118 0.00000000
C -9.44531250 0.70449984 0.00000000
C 9.44530773 -0.70450091 0.00000000
C -6.99528408 1.03862977 0.00000000
C 6.99527884 -1.03863037 0.00000000
C -10.38371086 -1.57286096 0.00000000

C 10.38370514 1.57286048 0.00000000
C -5.47686577 -0.90274304 0.00000000
C 5.47686005 0.90274173 0.00000000
C -10.76369190 1.20770228 0.00000000
C 10.76368713 -1.20770264 0.00000000
C -5.85674047 1.87935269 0.00000000
C 5.85673523 -1.87935376 0.00000000
H -10.23241329 -2.64811635 0.00000000
H 10.23240566 2.64811540 0.00000000
H -5.33027649 -1.97862923 0.00000000
H 5.33026886 1.97862792 0.00000000
H -10.90994263 2.28368711 0.00000000
H 10.90993786 -2.28368759 0.00000000
H -6.00853205 2.95449662 0.00000000
H 6.00852776 -2.95449758 0.00000000
C -11.67914391 -1.06567049 0.00000000
C 11.67913818 1.06567049 0.00000000
C -4.36550093 -0.06438924 0.00000000
C 4.36549520 0.06438758 0.00000000
C -11.87567043 0.37100893 0.00000000
C 11.87566471 -0.37100887 0.00000000
C -4.56643677 1.37154436 0.00000000
C 4.56643152 -1.37154591 0.00000000
C -12.83485413 -1.91612911 0.00000000
C 12.83484745 1.91612971 0.00000000
C -3.02918434 -0.56868756 0.00000000

C 3.02917838 0.56868529 0.00000000
C -13.21658802 0.88056803 0.00000000
C 13.21658325 -0.88056731 0.00000000
C -3.40303636 2.21517420 0.00000000
C 3.40303159 -2.21517611 0.00000000
H -12.68388176 -2.99316859 0.00000000
H 12.68387508 2.99316907 0.00000000
H -2.88808918 -1.64788556 0.00000000
H 2.88808250 1.64788330 0.00000000
H -13.36110401 1.95852780 0.00000000
H 13.36109924 -1.95852697 0.00000000
H -3.54865170 3.29301834 0.00000000
H 3.54864740 -3.29302025 0.00000000
C -14.09543991 -1.38647938 0.00000000
C 14.09543324 1.38648045 0.00000000
C -1.92513561 0.26085106 0.00000000
C 1.92513001 -0.26085377 0.00000000
C -14.28925800 0.03266053 0.00000000
C 14.28925323 -0.03265931 0.00000000
C -2.14609814 1.69066441 0.00000000
C 2.14609313 -1.69066703 0.00000000
H -14.96322536 -2.04089022 0.00000000
H 14.96321869 2.04089165 0.00000000
H -15.30041599 0.43142483 0.00000000
H 15.30041027 -0.43142313 0.00000000
H -1.29143643 2.35977221 0.00000000

H 1.29143167 -2.35977530 0.00000000
C -0.59145021 -0.32948795 0.00000000
C 0.59144425 0.32948473 0.00000000
H -0.58765703 -1.41819751 0.00000000
H 0.58765107 1.41819429 0.00000000

66yBP Structure Used for PPP Calculations

C 8.8126464405 0.0000000000 0.0000000000
C -8.8126464405 0.0000000000 0.0000000000
C 0.6754618538 0.0000000000 0.0000000000
C -0.6754618538 0.0000000000 0.0000000000
C 7.5997592132 0.0000000000 0.0000000000
C -7.5997592132 0.0000000000 0.0000000000
C 1.9039435613 0.0000000000 0.0000000000
C -1.9039435613 0.0000000000 0.0000000000
C 6.1769124108 0.0000000000 0.0000000000
C -6.1769124108 0.0000000000 0.0000000000
C 3.3101132040 0.0000000000 0.0000000000
C -3.3101132040 0.0000000000 0.0000000000
C 5.4725886874 -1.2381061438 0.0000000000
C -5.4725886874 -1.2381061438 0.0000000000
C 5.4725886874 1.2381061438 0.0000000000
C -5.4725886874 1.2381061438 0.0000000000
C 4.0214784718 -1.2414960540 0.0000000000
C -4.0214784718 -1.2414960540 0.0000000000
C 4.0214784718 1.2414960540 0.0000000000
C -4.0214784718 1.2414960540 0.0000000000
C 6.1528546455 -2.4750915850 0.0000000000
C -6.1528546455 -2.4750915850 0.0000000000
C 6.1528546455 2.4750915850 0.0000000000
C -6.1528546455 2.4750915850 0.0000000000
C 3.3482476722 -2.4788662615 0.0000000000

C -3.3482476722 -2.4788662615 0.0000000000
C 3.3482476722 2.4788662615 0.0000000000
C -3.3482476722 2.4788662615 0.0000000000
C 5.4778763675 -3.6918197777 0.0000000000
C -5.4778763675 -3.6918197777 0.0000000000
C 5.4778763675 3.6918197777 0.0000000000
C -5.4778763675 3.6918197777 0.0000000000
C 4.0282544584 -3.6942743126 0.0000000000
C -4.0282544584 -3.6942743126 0.0000000000
C 4.0282544584 3.6942743126 0.0000000000
C -4.0282544584 3.6942743126 0.0000000000
C 5.4735166467 -6.1287491908 0.0000000000
C -5.4735166467 -6.1287491908 0.0000000000
C 5.4735166467 6.1287491908 0.0000000000
C -5.4735166467 6.1287491908 0.0000000000
C 4.0414062574 -6.1309006058 0.0000000000
C -4.0414062574 -6.1309006058 0.0000000000
C 4.0414062574 6.1309006058 0.0000000000
C -4.0414062574 6.1309006058 0.0000000000
C 6.1666750376 -4.9500376145 0.0000000000
C -6.1666750376 -4.9500376145 0.0000000000
C 6.1666750376 4.9500376145 0.0000000000
C -6.1666750376 4.9500376145 0.0000000000
C 3.3442700178 -4.9541008366 0.0000000000
C -3.3442700178 -4.9541008366 0.0000000000
C 3.3442700178 4.9541008366 0.0000000000

C -3.3442700178 4.9541008366 0.0000000000
H 9.8791853511 0.0000000000 0.0000000000
H -9.8791853511 0.0000000000 0.0000000000
H 7.2386447019 -2.4700717770 0.0000000000
H -7.2386447019 -2.4700717770 0.0000000000
H 7.2386447019 2.4700717770 0.0000000000
H -7.2386447019 2.4700717770 0.0000000000
H 2.2621663549 -2.4804311889 0.0000000000
H -2.2621663549 -2.4804311889 0.0000000000
H 2.2621663549 2.4804311889 0.0000000000
H -2.2621663549 2.4804311889 0.0000000000
H 7.2542661597 -4.9448454951 0.0000000000
H -7.2542661597 -4.9448454951 0.0000000000
H 7.2542661597 4.9448454951 0.0000000000
H -7.2542661597 4.9448454951 0.0000000000
H 2.2566699811 -4.9524860584 0.0000000000
H -2.2566699811 -4.9524860584 0.0000000000
H 2.2566699811 4.9524860584 0.0000000000
H -2.2566699811 4.9524860584 0.0000000000
H 3.5118557631 7.0800143782 0.0000000000
H -3.5118557631 7.0800143782 0.0000000000
H 3.5118557631 -7.0800143782 0.0000000000
H -3.5118557631 -7.0800143782 0.0000000000
H 6.0058072668 7.0763213807 0.0000000000
H -6.0058072668 7.0763213807 0.0000000000
H 6.0058072668 -7.0763213807 0.0000000000

H -6.0058072668 -7.0763213807 0.0000000000

APPENDIX B

NORMAL MODE ANALYSIS DATA

Table B.1: $S_0 \rightarrow T_1$ normal mode analysis

Frequency (cm^{-1})	Displacement	Relaxation energy (eV)	Huang-Rhys factor
258.27	-0.274284	0.009227	0.288159
384.91	0.028754	0.000225	0.004720
618.13	0.028171	0.000558	0.007275
686.44	-0.030436	0.000803	0.009431
808.8	-0.070252	0.005936	0.059200
1053.01	-0.015454	0.000487	0.003729
1077.8	0.016900	0.000610	0.004565
1186.91	0.057338	0.008516	0.057871
1249.88	-0.114775	0.037839	0.244184
1331.11	-0.026976	0.002371	0.014365
1400.9	0.044943	0.007289	0.041965
1434.98	0.115998	0.050945	0.286352
1519.31	-0.052725	0.011799	0.062638
1548.22	0.084727	0.031639	0.164830
1592.35	-0.015619	0.001137	0.005761
2165.82	-0.012865	0.001427	0.005316

Table B.2: $S_0 \rightarrow S_1$ normal mode analysis.

Frequency (cm^{-1})	Displacement	Relaxation energy (eV)	Huang-Rhys factor
258.27	-0.177476	0.003863	0.120645
384.91	-0.013686	0.000051	0.001069
618.13	0.044277	0.001377	0.017972
686.44	-0.064420	0.003596	0.042248
808.80	-0.066978	0.005396	0.053810
1053.01	-0.022080	0.000994	0.007613
1077.80	0.014811	0.000469	0.003506
1186.91	0.056577	0.008291	0.056345
1249.88	-0.091255	0.023920	0.154361
1400.90	0.067828	0.016601	0.095582
1434.98	0.086064	0.028045	0.157634
1519.31	-0.027047	0.003105	0.016483
1548.22	0.062341	0.017129	0.089234
1592.35	-0.022252	0.002308	0.011693

APPENDIX C

ANALYTIC FITS OF NEWNS MODEL POTENTIAL ENERGY SURFACES

The analytic fits of the neutral and anionic diabatic potentials, V_{nn} and V_{aa} , respectively, along their coupling (V_{na}) is given below. The potentials are expressed in units of eV, while position coordinates are in units of Å.

$$V_{nn} = \frac{22.819}{Z} e^{-1.293Z} + 6.612(1 - e^{-3.200(r-1.151)})^2 \quad (\text{C.1})$$

$$V_{aa} = \frac{34.124}{Z} e^{-2.029Z} - \left(\frac{6.803}{Z_{coc} - 0.150} (1 - e^{-2.362(Z_{coc} - 0.150)}) \right) + 5.143(1 - e^{-2.400(r-1.271)})^2 + 6.675 \quad (\text{C.2})$$

$$V_{na} = 5.0e^{-0.445Z - 0.162r} - 0.049 \quad (\text{C.3})$$

Z_{coc} in Equation C.2 is the center-of-charge coordinate which gives the average position of the additional electron relative to the metal surface. It is estimated through the use of Pauling electronegativities and is given in Equation 4.4.

BIBLIOGRAPHY

- [1] Fuemmeler, E. G.; Sanders, S. N.; Pun, A. B.; Kumarasamy, E.; Zeng, T.; Miyata, K.; Steigerwald, M. L.; Zhu, X.-Y.; Sfeir, M. Y.; Campos, L. M.; Ananth, N. *ACS Cent. Sci.* **2016**, *2*, 316–324.
- [2] Kumarasamy, E. et al. *J. Am. Chem. Soc.* **2017**, *139*, 1248812494.
- [3] Hele, T. J. H.; Fuemmeler, E. G.; Sanders, S. N.; Kumarasamy, E.; Sfeir, M. Y.; Campos, L. M.; Ananth, N. (*in preparation*) **2018**,
- [4] Swenberg, C.; Stacy, W. *Chemical Physics Letters* **1968**, *2*, 327 – 328.
- [5] Marciniak, H.; Fiebig, M.; Huth, M.; Schiefer, S.; Nickel, B.; Selmaier, F.; Lochbrunner, S. *Phys. Rev. Lett.* **2007**, *99*, 176402.
- [6] Agostini, G.; Corvaja, C.; Giacometti, G.; Pasimeni, L. *Chemical Physics* **1993**, *173*, 177 – 186.
- [7] Ma, L.; Zhang, K.; Kloc, C.; Sun, H.; Michel-Beyerle, M. E.; Gurzadyan, G. G. *Phys. Chem. Chem. Phys.* **2012**, *14*, 8307–8312.
- [8] Katoh, R.; Hashimoto, M.; Takahashi, A.; Sonoda, Y.; Yago, T.; Wakasa, M. *The Journal of Physical Chemistry C* **2017**, *121*, 25666–25671.
- [9] Schwerin, A. F. et al. *The Journal of Physical Chemistry A* **2010**, *114*, 1457–1473.
- [10] Johnson, J. C.; Akdag, A.; Zamadar, M.; Chen, X.; Schwerin, A. F.; Paci, I.; Smith, M. B.; Havlas, Z.; Miller, J. R.; Ratner, M. A.; Nozik, A. J.; Michl, J. *The Journal of Physical Chemistry B* **2013**, *117*, 4680–4695, PMID: 23383860.

- [11] Kumarasamy, E.; Sanders, S. N.; Pun, A. B.; Vaselabadi, S. A.; Low, J. Z.; Sfeir, M. Y.; Steigerwald, M. L.; Stein, G. E.; Campos, L. M. *Macromolecules* **2016**, *49*, 1279–1285.
- [12] Yamamoto, Y.; Wakamatsu, K.; Iwanaga, T.; Sato, H.; Toyota, S. *Chem.–Asian J.* **2016**, *11*, 1370–1375.
- [13] Lehnherr, D.; Murray, A.; McDonald, R.; Tykwinski, R. *Angew. Chem., Int. Ed.* **2010**, *49*, 6190–6194.
- [14] Barlier, V. S.; Schlenker, C. W.; Chin, S. W.; Thompson, M. E. *Chem. Commun. (Camb)* **2011**, *47*, 3754–6.
- [15] Akiyama, S.; Misumi, S.; Nakagawa, M. *B. Chem. Soc. Jpn.* **1960**, *33*, 1293–1298.
- [16] Rüdiger, E. C.; Porz, M.; Schaffroth, M.; Rominger, F.; Bunz, U. H. F. *Chemistry* **2014**, *20*, 12725–8.
- [17] Long, T. M.; Swager, T. M. *Adv. Mater.* **2001**, *13*, 601–604.
- [18] Bhola, R.; Payamyar, P.; Murray, D. J.; Kumar, B.; Teator, A. J.; Schmidt, M. U.; Hammer, S. M.; Saha, A.; Sakamoto, J.; Schlüter, A. D.; King, B. T. *J. Am. Chem. Soc.* **2013**, *135*, 14134–14141.
- [19] Cook, J. D.; Carey, T. J.; Damrauer, N. H. *J. Phys. Chem. A* **2016**, *120*, 4473.
- [20] Bula, R.; Fingerle, M.; Ruff, A.; Speiser, B.; Maichle-Mössmer, C.; Bettinger, H. F. *Angew. Chem., Int. Ed.* **2013**, *52*, 11647–11650.
- [21] Geyer, F. L.; Brosius, V.; Bunz, U. H. F. *J. Org. Chem.* **2015**, *80*, 12166–76.
- [22] Balandier, J.-Y.; Quist, F.; Stas, S.; Tylleman, B.; Ragoen, C.; Mayence, A.; Bouzakraoui, S.; Cornil, J.; Geerts, Y. H. *Org. Lett.* **2011**, *13*, 548–551.

- [23] Gu, P.-Y.; Gao, J.; Wang, C.; Zhang, Q. *RSC Adv.* **2015**, *5*, 80307–80310.
- [24] Ananth, N. *The Journal of Chemical Physics* **2013**, *139*, 124102.
- [25] Helgaker, T.; Jorgensen, P.; Olsen, J. *Molecular Electronic-Structure Theory*; Wiley: Chichester, 2000.
- [26] Baer, M. *Beyond Born-Oppenheimer Conical Intersections and Electronic Nonadiabatic Coupling Terms*; Wiley: Hoboken, 2006.
- [27] Macias, A.; Riera, A. *Journal of Physics B: Atomic and Molecular Physics* **1978**, *11*, L489.
- [28] Werner, H.; Meyer, W. *The Journal of Chemical Physics* **1981**, *74*, 5802–5807.
- [29] Ruedenberg, K.; Atchity, G. J. *The Journal of Chemical Physics* **1993**, *99*, 3799–3803.
- [30] Smith, M. B.; Michl, J. *Chem. Rev.* **2010**, *110*, 6891–6936.
- [31] Smith, M. B.; Michl, J. *Annu Rev Phys Chem* **2013**, *64*, 361–86.
- [32] Berkelbach, T. C.; Hybertsen, M. S.; Reichman, D. R. *The Journal of Chemical Physics* **2013**, *138*, –.
- [33] Berkelbach, T. C.; Hybertsen, M. S.; Reichman, D. R. *The Journal of Chemical Physics* **2013**, *138*, –.
- [34] Berkelbach, T. C.; Hybertsen, M. S.; Reichman, D. R. *The Journal of Chemical Physics* **2014**, *141*, –.
- [35] Müller, A. M.; Avlasevich, Y. S.; Müllen, K.; Bardeen, C. J. *Chemical Physics Letters* **2006**, *421*, 518 – 522.

- [36] Müller, A. M.; Avlasevich, Y. S.; Schoeller, W. W.; Müllen, K.; Bardeen, C. J. *Journal of the American Chemical Society* **2007**, *129*, 14240–14250, PMID: 17958421.
- [37] Zirzlmeyer, J.; Lehnherr, D.; Coto, P. B.; Chernick, E. T.; Casillas, R.; Basel, B. S.; Thoss, M.; Tykwinski, R. R.; Guldi, D. M. *Proc. Natl. Acad. Sci. U.S.A.* **2015**, *112*, 5325–30.
- [38] Varnavski, O.; Abeyasinghe, N.; Aragón, J.; Serrano-Pérez, J. J.; Ortí, E.; López Navarrete, J. T.; Takimiya, K.; Casanova, D.; Casado, J.; Goodson, T. *The Journal of Physical Chemistry Letters* **2015**, *6*, 1375–1384.
- [39] Busby, E.; Xia, J.; Wu, Q.; Low, J. Z.; Song, R.; Miller, J. R.; Zhu, X.-Y.; Campos, L. M.; Sfeir, M. Y. *Nat Mater* **2015**, *14*, 426–433.
- [40] Aryanpour, K.; Shukla, A.; Mazumdar, S. *J. Phys. Chem. C* **2015**, *119*, 6966–6979.
- [41] Chan, W.-L.; Berkelbach, T. C.; Provorse, M. R.; Monahan, N. R.; Tritsch, J. R.; Hybertsen, M. S.; Reichman, D. R.; Gao, J.; Zhu, X.-Y. *Accounts of Chemical Research* **2013**, *46*, 1321–1329, PMID: 23581494.
- [42] Sanders, S. N.; Kumarasamy, E.; Pun, A. B.; Trinh, M. T.; Choi, B.; Xia, J.; Taffet, E. J.; Low, J. Z.; Miller, J. R.; Roy, X.; Zhu, X.-Y.; Steigerwald, M. L.; Sfeir, M. Y.; Campos, L. M. *J. Am. Chem. Soc.* **2015**, *137*, 8965–72.
- [43] Becke, A. D. *The Journal of Chemical Physics* **1993**, *98*, 5648–5652.
- [44] Lee, C.; Yang, W.; Parr, R. G. *Phys. Rev. B* **1988**, *37*, 785–789.
- [45] Hehre, W. J.; Ditchfield, R.; Pople, J. A. *The Journal of Chemical Physics* **1972**, *56*, 2257–2261.

- [46] Kaur, I.; Jia, W.; Kopreski, R. P.; Selvarasah, S.; Dokmeci, M. R.; Pramanik, C.; McGruer, N. E.; Miller, G. P. *Journal of the American Chemical Society* **2008**, *130*, 16274–16286, PMID: 19006312.
- [47] Zeng, T.; Hoffmann, R.; Ananth, N. *J. Am. Chem. Soc.* **2014**, *136*, 5755–5764.
- [48] Granovsky, A. A. *The Journal of Chemical Physics* **2011**, *134*, –.
- [49] Nakano, H.; Uchiyama, R.; Hirao, K. *Journal of Computational Chemistry* **2002**, *23*, 1166–1175.
- [50] Ebisuzaki, R.; Watanabe, Y.; Nakano, H. *Chemical Physics Letters* **2007**, *442*, 164 – 169.
- [51] Witek, H. A.; Choe, Y.-K.; Finley, J. P.; Hirao, K. *Journal of Computational Chemistry* **2002**, *23*, 957–965.
- [52] Stevens, W. J.; Basch, H.; Krauss, M. *The Journal of Chemical Physics* **1984**, *81*, 6026–6033.
- [53] Nakamura, H.; Truhlar, D. G. *The Journal of Chemical Physics* **2001**, *115*, 10353–10372.
- [54] Nakamura, H.; Truhlar, D. G. *The Journal of Chemical Physics* **2002**, *117*, 5576–5593.
- [55] Barone, V.; Cossi, M. *The Journal of Physical Chemistry A* **1998**, *102*, 1995–2001.
- [56] Cossi, M.; Rega, N.; Scalmani, G.; Barone, V. *Journal of Computational Chemistry* **2003**, *24*, 669–681.

- [57] Schmidt, M. W.; Baldrige, K. K.; Boatz, J. A.; Elbert, S. T.; Gordon, M. S.; Jensen, J. H.; Koseki, S.; Matsunaga, N.; Nguyen, K. A.; Su, S.; Windus, T. L.; Dupuis, M.; Montgomery, J. A. *J. Comput. Chem.* **1993**, *14*, 1347–1363.
- [58] Gordon, M. S.; Schmidt, M. W. In *Theory and Applications of Computational Chemistry*; Dykstra, C. E., Frenking, G., Kim, K. S., Scuseria, G. E., Eds.; Elsevier: Amsterdam, 2005; pp 1167 – 1189.
- [59] Maliakal, A.; Raghavachari, K.; Katz, H.; Chandross, E.; Siegrist, T. *Chemistry of Materials* **2004**, *16*, 4980–4986.
- [60] Parker, S. M.; Seideman, T.; Ratner, M. A.; Shiozaki, T. *The Journal of Physical Chemistry C* **2014**, *118*, 12700–12705.
- [61] Zeng, T.; Ananth, N.; Hoffmann, R. *J. Am. Chem. Soc.* **2014**, *136*, 12638–12647.
- [62] Havenith, R. W.; de Gier, H. D.; Broer, R. *Molecular Physics* **2012**, *110*, 2445–2454.
- [63] Alguire, E. C.; Subotnik, J. E.; Damrauer, N. H. *The Journal of Physical Chemistry A* **2015**, *119*, 299–311, PMID: 25522781.
- [64] Tao, G. *The Journal of Physical Chemistry C* **2014**, *118*, 17299–17305.
- [65] Feng, X.; Luzanov, A. V.; Krylov, A. I. *The Journal of Physical Chemistry Letters* **2013**, *4*, 3845–3852.
- [66] Beljonne, D.; Yamagata, H.; Brédas, J. L.; Spano, F. C.; Olivier, Y. *Phys. Rev. Lett.* **2013**, *110*, 226402.

- [67] Yamagata, H.; Norton, J.; Hontz, E.; Olivier, Y.; Beljonne, D.; Brédas, J. L.; Silbey, R. J.; Spano, F. C. *The Journal of Chemical Physics* **2011**, *134*, –.
- [68] Greyson, E. C.; Stepp, B. R.; Chen, X.; Schwerin, A. F.; Paci, I.; Smith, M. B.; Akdag, A.; Johnson, J. C.; Nozik, A. J.; Michl, J.; Ratner, M. A. *The Journal of Physical Chemistry B* **2010**, *114*, 14223–14232, PMID: 20025238.
- [69] Beens, H.; Weller, A. *Chemical Physics Letters* **1969**, *3*, 666 – 668.
- [70] Grabner, G.; Rechthaler, K.; Köhler, G. *The Journal of Physical Chemistry A* **1998**, *102*, 689–696.
- [71] Topaler, M.; Makri, N. *Chem. Phys. Lett.* **1993**, *210*, 448–457.
- [72] Topaler, M.; Makri, N. *J. Chem. Phys.* **1994**, *101*, 7500–7519.
- [73] Makri, N. *J. Math. Phys.* **1995**, *36*, 2430–2457.
- [74] Sim, E.; Makri, N. *Comput. Phys. Commun.* **1997**, *99*, 335–354.
- [75] Makri, N. *J. Phys. Chem. A* **1998**, *102*, 4414–4427.
- [76] Hückel, E. *Zeitschrift für Physik* **1930**, *60*, 423–456.
- [77] Thomas, W. *Naturwissenschaften* **1925**, *13*, 627–627.
- [78] Reiche, F.; Thomas, W. *Zeitschrift für Physik* **1925**, *34*, 510–525.
- [79] Kuhn, W. *Zeitschrift für Physik* **1925**, *33*, 408–412.
- [80] Pople, J. A. *Trans. Faraday Soc.* **1953**, *49*, 1375–1385.
- [81] Pople, J. A. *P. Phys. Soc. Lond.. Section A* **1955**, *68*, 81.
- [82] Pariser, R.; Parr, R. G. *J. Chem. Phys.* **1953**, *21*, 466–471.

- [83] Pariser, R. *J. Chem. Phys.* **1956**, *24*, 250–268.
- [84] Sony, P.; Shukla, A. *Phys. Rev. B* **2007**, *75*, 155208.
- [85] Hashimoto, T.; Nakano, H.; Hirao, K. *J. Chem. Phys.* **1996**, *104*, 6244–6258.
- [86] Kawashima, Y.; Hashimoto, T.; Nakano, H.; Hirao, K. *Theor. Chem. Acc.* **1999**, *102*, 49–64.
- [87] M. Kasha, H. R. R.; El-Bayoumi, M. A. *Pure Appl. Chem.* **1965**, *11*, 371–392.
- [88] Kazmaier, P. M.; Hoffmann, R. *J. Am. Chem. Soc.* **1994**, *116*, 9684–9691.
- [89] Hanson, K.; Roskop, L.; Djurovich, P. I.; Zahariev, F.; Gordon, M. S.; Thompson, M. E. *J. Am. Chem. Soc.* **2010**, *132*, 16247–16255.
- [90] Mishra, A.; Fischer, M.; Bäuerle, P. *Angew. Chem., Int. Ed.* **2009**, *48*, 2474–2499.
- [91] Zollinger, H. *Color chemistry: syntheses, properties, and applications of organic dyes and pigments*; John Wiley & Sons, 2003.
- [92] Christie, R. *Colour Chemistry*; Royal Society of Chemistry: Cambridge, UK, 2015.
- [93] Pun, A. B.; Sanders, S. N.; Kumarasamy, E.; Sfeir, M. Y.; Congreve, D. N.; Campos, L. M. *Advanced Materials* **2017**, *29*, 1701416–n/a, 1701416.
- [94] Sanders, S. N.; Kumarasamy, E.; Pun, A. B.; Steigerwald, M. L.; Sfeir, M. Y.; Campos, L. M. *Angew. Chem., Int. Ed.* **2016**, *55*, 3373–7.
- [95] Lukman, S.; Musser, A. J.; Chen, K.; Athanasopoulos, S.; Yong, C. K.; Zeng, Z.; Ye, Q.; Chi, C.; Hodgkiss, J. M.; Wu, J.; Friend, R. H.; Greenham, N. C. *Adv. Funct. Mater.* **2015**, *25*, 5452–5461.

- [96] Friedel, R. A.; Orchin, M.; Reggel, L. *J. Am. Chem. Soc.* **1948**, *70*, 199–204.
- [97] Forrest, S. R. *MRS Bulletin* **2005**, *30*, 28–32.
- [98] Coulson, C. A. *P. Phys. Soc. Lond.* **1948**, *60*, 257.
- [99] Dewar, M. J. S.; Longuet-Higgins, H. C. *P. Phys. Soc. Lond.. Section A* **1954**, *67*, 795.
- [100] Akiyama, S.; Nakagawa, M. *B. Chem. Soc. Jpn.* **1960**, *33*, 1291–1293.
- [101] Tanaka, J. *B. Chem. Soc. Jpn.* **1965**, *38*, 86–102.
- [102] Clar, E.; Schmidt, W. *Tetrahedron* **1979**, *35*, 2673 – 2680.
- [103] Halasinski, T. M.; Hudgins, D. M.; Salama, F.; Allamandola, L. J.; Bally, T. *J. Phys. Chem. A* **2000**, *104*, 7484–7491.
- [104] Payne, M. M.; Parkin, S. R.; Anthony, J. E. *J. Am. Chem. Soc.* **2005**, *127*, 8028–8029, PMID: 15926823.
- [105] Lehnherr, D.; Gao, J.; Hegmann, F. A.; Tykwinski, R. R. *Org. Lett.* **2008**, *10*, 4779–4782.
- [106] Hajgató, B.; Szieberth, D.; Geerlings, P.; De Proft, F.; Deleuze, M. S. *J. Chem. Phys.* **2009**, *131*.
- [107] Yamagata, H.; Norton, J.; Hontz, E.; Olivier, Y.; Beljonne, D.; Brdas, J. L.; Silbey, R. J.; Spano, F. C. *J. Chem. Phys.* **2011**, *134*, 204703.
- [108] Kurashige, Y.; Yanai, T. *B. Chem. Soc. Jpn.* **2014**, *87*, 1071–1073.
- [109] Suzuki, S.; Fujii, T.; Baba, H. *J. Mol. Spectrosc.* **1973**, *47*, 243–251.
- [110] Koutecký, J. *Chem. Phys. Lett.* **1967**, *1*, 249 – 250.

- [111] Paci, I.; Johnson, J. C.; Chen, X.; Rana, G.; Popovi, D.; David, D. E.; Nozik, A. J.; Ratner, M. A.; Michl, J. *Journal of the American Chemical Society* **2006**, *128*, 16546–16553, PMID: 17177404.
- [112] Aryanpour, K.; Muñoz, J. A.; Mazumdar, S. J. *Phys. Chem. C* **2013**, *117*, 4971–4979.
- [113] Venkataraman, L.; Klare, J. E.; Nuckolls, C.; Hybertsen, M. S.; Steigerwald, M. L. *Nature* **2006**, *442*, 904–907.
- [114] Geskin, V. M.; Lambert, C.; Brédas, J.-L. *J. Am. Chem. Soc.* **2003**, *125*, 15651–15658.
- [115] Mataga, N.; Nishimoto, K. *Z. Phys. Chem.* **1957**, *13*, 140–157.
- [116] Aryanpour, K.; Psiachos, D.; Mazumdar, S. *Phys. Rev. B* **2010**, *81*, 085407.
- [117] Coulson, C. A.; Rushbrooke, G. S. *Math. Proc. Cambridge* **1940**, *36*, 193–200.
- [118] Szabo, A.; Ostlund, N. *Modern Quantum Chemistry: Introduction to Advanced Electronic Structure Theory*; Dover Books on Chemistry; Dover Publications, 1989.
- [119] Li, X.; Parrish, R. M.; Liu, F.; Kokkila Schumacher, S. I. L.; Martínez, T. J. *Journal of Chemical Theory and Computation* **2017**, *13*, 3493–3504, PMID: 28617595.
- [120] Atkins, P. W.; Friedman, R. S. *Molecular quantum mechanics*; Oxford University Press, 2011.
- [121] Löwdin, P. J. *Chem. Phys.* **1951**, *19*, 1396–1401.
- [122] Robinson, G. W. *J. Chem. Phys.* **1967**, *46*, 572.

- [123] Lee, D.-C.; Cao, B.; Jang, K.; Forster, P. M. *J. Mater. Chem.* **2010**, *20*, 867–873.
- [124] Gawrys, P.; Marszalek, T.; Bartnik, E.; Kucinska, M.; Ulanski, J.; Zagorska, M. *Org. Lett.* **2011**, *13*, 6090–6093.
- [125] Clayden, J.; Greeves, N.; Warren, S.; Wothers, P. *Organic chemistry*; Oxford University Press, 2001.
- [126] Zirzmeier, J.; Casillas, R.; Reddy, S. R.; Coto, P. B.; Lehnerr, D.; Chernenick, E. T.; Papadopoulos, I.; Thoss, M.; Tykwinski, R. R.; Guldi, D. M. *Nanoscale* **2016**, *8*, 10113–23.
- [127] Krger, B. C.; Meyer, S.; Kandratsenka, A.; Wodtke, A. M.; Schfer, T. *The Journal of Physical Chemistry Letters* **2016**, *7*, 441–446, PMID: 26760437.
- [128] Krger, B. C.; Bartels, N.; Bartels, C.; Kandratsenka, A.; Tully, J. C.; Wodtke, A. M.; Schfer, T. *The Journal of Physical Chemistry C* **2015**, *119*, 3268–3272.
- [129] Werdecker, J.; Shirhatti, P. R.; Golibrzuch, K.; Bartels, C.; Wodtke, A. M.; Harding, D. J. *The Journal of Physical Chemistry C* **2015**, *119*, 14722–14727.
- [130] Wodtke, A. M. *Chem. Soc. Rev.* **2016**, *45*, 3641–3657.
- [131] Lang, N. D.; Kohn, W. *Phys. Rev. B* **1973**, *7*, 3541–3550.
- [132] Shenvi, N.; Roy, S.; Parandekar, P.; Tully, J. *The Journal of Chemical Physics* **2006**, *125*, 154703.
- [133] Roy, S.; Shenvi, N. A.; Tully, J. C. *The Journal of Chemical Physics* **2009**, *130*, 174716.
- [134] Shenvi, N.; Roy, S.; Tully, J. C. *The Journal of Chemical Physics* **2009**, *130*, 174107.

- [135] Shenvi, N.; Roy, S.; Tully, J. C. *Science* **2009**, *326*, 829–832.
- [136] News, D. M. *Phys. Rev.* **1969**, *178*, 1123–1135.
- [137] McCarthy, M.; Allington, J. W.; Griffith, K. *Chemical Physics Letters* **1998**, *289*, 156 – 159.
- [138] Michaelson, H. B. *Journal of Applied Physics* **1977**, *48*, 4729–4733.
- [139] Smith, N. V.; Chen, C. T.; Weinert, M. *Phys. Rev. B* **1989**, *40*, 7565–7573.
- [140] Wilson, K. G. *Rev. Mod. Phys.* **1975**, *47*, 773–840.
- [141] Ramchandani, M. G. *Journal of Physics C: Solid State Physics* **1970**, *3*, S1.
- [142] Piccitto, G.; Siringo, F.; Baldo, M.; Pucci, R. *Surface Science* **1986**, *167*, 437 – 450.
- [143] Gajdoš, M.; Hafner, J.; Eichler, A. *Journal of Physics: Condensed Matter* **2006**, *18*, 13.
- [144] Ekert, A.; Knight, P. L. *American Journal of Physics* **1995**, *63*, 415–423.
- [145] White, S. R. *Phys. Rev. Lett.* **1992**, *69*, 2863–2866.
- [146] Knizia, G.; Chan, G. K.-L. *Journal of Chemical Theory and Computation* **2013**, *9*, 1428–1432, PMID: 26587604.
- [147] Condon, E. U. *Phys. Rev.* **1930**, *36*, 1121–1133.
- [148] Wouters, S.; Jimnez-Hoyos, C. A.; Sun, Q.; Chan, G. K.-L. *Journal of Chemical Theory and Computation* **2016**, *12*, 2706–2719, PMID: 27159268.
- [149] MacDonald, J. K. L. *Phys. Rev.* **1933**, *43*, 830–833.

- [150] Church, M. S.; Hele, T. J. H.; Ezra, G. S.; Ananth, N. *The Journal of Chemical Physics* **2018**, *148*, 102326.
- [151] Sun, X.; Miller, W. H. *The Journal of Chemical Physics* **1997**, *106*, 6346–6353.
- [152] Colbert, D. T.; Miller, W. H. *The Journal of Chemical Physics* **1992**, *96*, 1982–1991.
- [153] Kaduk, B.; Kowalczyk, T.; Van Voorhis, T. *Chemical Reviews* **2012**, *112*, 321–370, PMID: 22077560.
- [154] Boggio-Pasqua, M.; Bearpark, M. J.; Klene, M.; Robb, M. A. *The Journal of Chemical Physics* **2004**, *120*, 7849–7860.
- [155] Piris, M.; Matxain, J. M.; Lopez, X.; Ugalde, J. M. *The Journal of Chemical Physics* **2010**, *132*, 031103.
- [156] Mazziotti, D. A. *Accounts of Chemical Research* **2006**, *39*, 207–215, PMID: 16548509.